The Astrophysical Journal, 969:101 (20pp), 2024 July 10 https://doi.org/10.3847/1538-4357/ad3def

Modeling Ionized Gas in the Small Magellanic Cloud: The Wolf–Rayet Nebula N76

Elizabeth Tarantino[1,2], Alberto D. Bolatto[2], Rémy Indebetouw[3,4], Mónica Rubio[5], Karin M. Sandstrom[6], J.-D T. Smith[7], Daniel Stapleton[1,2], and Mark Wolfire[2]
[1] Space Telescope Science Institute, 3700 San Martin Drive, Baltimore, MD 21218, USA; etarantino@stsci.edu
[2] Department of Astronomy, University of Maryland, College Park, MD 20742, USA
[3] Department of Astronomy, University of Virginia, Charlottesville, VA 22904, USA
[4] National Radio Astronomy Observatory, 520 Edgemont Road, Charlottesville, VA 22903, USA
[5] Departamento de Astronomía, Universidad de Chile, Casilla 36-D, Santiago, Chile
[6] Center for Astrophysics & Space Sciences, Department of Physics, University of California, San Diego, 9500 Gilman Drive, San Diego, CA 92093, USA
[7] Department of Physics & Astronomy, University of Toledo, Toledo, OH 43606, USA
Received 2023 April 25; revised 2024 April 2; accepted 2024 April 10; published 2024 July 10

Abstract

We present `Cloudy` modeling of infrared emission lines in the Wolf–Rayet (WR) nebula N76 caused by one of the most luminous and hottest WR stars in the low metallicity Small Magellanic Cloud. We use spatially resolved mid-infrared Spitzer/InfRared Spectrograph and far-infrared Herschel/PACS spectroscopy to establish the physical conditions of the ionized gas. The spatially resolved distribution of the emission allows us to constrain properties much more accurately than using spatially integrated quantities. We construct models with a range of constant hydrogen densities between $n_H = 4$–$10\ cm^{-3}$ and a stellar wind-blown cavity of 10 pc, which reproduces the intensity and shape of most ionized gas emission lines, including the high ionization lines [O IV] and [Ne V], as well as [S III], [S IV], [O III], and [Ne III]. Our models suggest that the majority of [Si II] emission (91%) is produced at the edge of the H II region around the transition between ionized and atomic gas while very little of the [C II] (<5%) is associated with the ionized gas. The physical conditions of N76 are characterized by a hot HII region with a maximum electron temperature of $T_e \sim 24{,}000$ K, electron densities that range from $n_e \sim 4$ to $12\ cm^{-3}$, and high ionization parameters of $\log(U) \sim -1.15$ to –1.77. By analyzing a low-metallicity WR nebula with a single ionization source, this work gives valuable insights into the impact WR stars have on the galaxy-integrated ionized gas properties in nearby dwarf galaxies.

Unified Astronomy Thesaurus concepts: Interstellar medium (847); H II regions (694); Small Magellanic Cloud (1468); Wolf-Rayet stars (1806); Photoionization (2060)

1. Introduction

Massive stars inject energy into the surrounding gas, heating and influencing the chemistry of their nearby interstellar medium (ISM). The effects massive stars have on the ISM depend on a variety of factors, including the metallicity of the surrounding material. Lower metallicity stars have harder radiation fields and a decreased mass-loss rate (e.g., Hurley et al. 2000; Vink et al. 2001). At the same time, the low-metallicity ISM contains less dust (e.g., Galliano et al. 2021), which consequently leads to a more porous structure with a lower H II region effective covering fraction allowing radiation fields to penetrate deeper into the ISM (e.g., Poglitsch et al. 1995; Cormier et al. 2015, 2019). The chemistry and physical processes governing the interaction between massive stars are thus highly affected by the metallicity of the medium.

Investigation of ionized gas tracers is used to determine the properties of the ionized gas across galaxies. In particular, the infrared (IR) lines such as [Ne II], [S III], [O III], [Ne III], and [S IV], accessed by the Spitzer, Herschel, and James Webb space telescopes trace a variety of conditions in the ISM, including the ionizing radiation field strength and hardness, the ionization parameter, the density and temperature of the ionized gas, and the heating mechanism of the gas (e.g., Baldwin et al. 1981; Kaufman et al. 2006; Cormier et al. 2015, 2019; Polles et al. 2019). The IR fine-structure lines are less affected by extinction and dust attenuation than optical lines and are therefore ideal for studying star-forming regions.

Previous studies of mostly spatially unresolved infrared spectroscopy in low-metallicity star-forming galaxies find harder radiation fields, extended, bright [O III] emission, and an overall more porous structure (Hunt et al. 2010; Cormier et al. 2015, 2019). The majority of spectra analyzed in these studies, however, are unresolved and contain emission from the different phases of the ISM and a variety of HII regions that vary in properties (density, ionization parameter, stellar population, etc.) blended into one beam or observation. Spatially resolved studies that focus on individual HII regions, on the other hand, bring additional information and can be considerably more powerful at constraining physical conditions. Of course, they can only be carried out in nearby sources. The Small Magellanic Cloud (SMC), at one-fifth solar metallicity and only 63 kpc (Dufour 1984; Russell & Dopita 1992) away provides the ideal laboratory for studying the low-metallicity ionized gas in spatially resolved detail.

This paper focuses on studying the ionized gas emission around the class of the hottest and most luminous stars in the local Universe, a Wolf–Rayet (WR) star. After an O-type star loses its hydrogen-rich envelope (either from binary stripping and accretion or via stellar winds removing the outer layers of the star), the inner, hot core is exposed and forms a WR star (Crowther & Hadfield 2006). WR stars are characterized by effective temperatures of $T_* \sim 50$–110 kK, luminosities of $\log L \sim 5$–$6.2\ L_\odot$, have strong stellar winds with velocities

that range from $v_\infty \sim 1500$–5000 km s^{-1}, and mass outflow rates of $\dot{M} \sim 10^{-4}$–10^{-5} $M_\odot$ yr^{-1} (Crowther & Hadfield 2006). These stellar winds compress the surrounding material, forming a stellar windblown bubble (Weaver et al. 1977). Simultaneously, the bright ultraviolet (UV) flux from the WR star creates a highly ionized HII region, forming a structure often called a WR nebula, a subclass of HII regions (e.g., Chu 1981). Since WR stars inject massive amounts of energy into the surrounding medium, they can have a profound influence on shaping the nearby ISM and energy exchange in stellar clusters (e.g., Sokal et al. 2016).

This paper studies the WR nebula N76 that harbors one of the hottest, most luminous WR stars in the SMC (Shenar et al. 2016). First classified by Henize (1956) as an HII region, Garnett et al. (1991) identified broad He II emission in N76, indicative of a WR nebula. N76 is powered by a well-studied binary system consisting of a WN4 and an O6 I(f) star (Niemela et al. 2002; Shenar et al. 2016). The goal of this work is to model the physical conditions of the ionized gas in N76 using mid and far-infrared spectroscopy and the `Cloudy` photoionization code (Ferland et al. 2017) to provide a detailed, resolved view of the impact the most energetic stars have on the metal-poor ISM. Many low-metallicity dwarf galaxies that have been studied in the past (Wu et al. 2006; Hunt et al. 2010; Cormier et al. 2015, 2019) contain a large number of WR stars and are undergoing a burst of active star formation, but these galaxies are too far away to examine the specific impact of WR stars in detail. Therefore N76 provides the ideal case study to isolate the impact WR stars have on the low-metallicity ISM due to its proximity and simple, well-characterized single ionization source.

Observations of Milky Way WR nebulae show that they vary in morphology, but often appear as thin, bubble structures, or disrupted shells (Chu 1981; Chu et al. 1983; Toalá et al. 2015). In particular, the well-studied WR nebula NGC 6888 shows a double shell model with a denser inner shell ($n_e \sim 400$ cm^{-3}) and a thinner outer shell ($n_e \sim 180$ cm^{-3}) (Fernández-Martín et al. 2012; Rubio et al. 2020). Due to the rarity of WR nebulae (e.g., Conti & Massey 1989; Hainich et al. 2014; Neugent et al. 2018), there have been few observations investigating the properties of WR nebulae at low metallicities. It is possible that the lower dust abundance and harder radiation fields at low metallicities will allow high-energy photons to penetrate deeper into the low-metallicity ISM, forming larger, lower-density nebulae with high ionizing photon escape fractions.

Further, understanding how WR stars directly affect their surrounding environment and host galaxies is essential to deciphering the nature of extreme emission line galaxies (EELGs). These are local analogs to galaxies during the Epoch of Reionization, characterized by bright emission lines from high ionization species (such as [O III], C III], C IV, He II, and [Ne V]), low metallicities, and highly ionized gas (e.g., Atek et al. 2011; Maseda et al. 2013; Rigby et al. 2015; Senchyna et al. 2017; Berg et al. 2019; Olivier et al. 2022). The ionization source for the extreme emission found in these galaxies is unclear, but ultraluminous X-ray sources and radiation from WR stars are possible explanations. The observations of N76 presented in this work will directly test whether low-metallicity WR nebula can produce the high ionization species ([O IV] and [Ne V]) associated with EELGs.

Below we outline the sections of this paper. In Section 2, we describe the Spitzer and Herschel observations and the methods of producing line-integrated spatially resolved emission line maps. Section 3 describes the `Cloudy` photoionization model input conditions and N76 geometry. We then compare the photoionization models to the spatially resolved IR data in Section 4. We discuss the implications of these results, putting N76 in context with other low-metallicity galaxies and WR nebulae in Section 5. Lastly, our conclusions are described in Section 6.

2. Observations

2.1. Spitzer InfRared Spectrograph Observations and Spectral Line Images

The Spitzer data come from the InfRared Spectrograph (IRS) as part of the Spitzer Spectroscopic Survey of the Small Magellanic Cloud (S^{4}MC). The full observations are described by Sandstrom et al. (2012), but we summarize them briefly here. We downloaded the raw basic calibrated data files from the Spitzer Heritage Archive from project GO 30491 (PI: A. Bolatto) with pipeline version S18.18. We use the long–low (LL) and short-low (SL) modules of the IRS to cover the 5.2–38.4 μm range with a resolving power ranging from $R \sim 60$–120 (coverage of the modules is shown in Figure 3 of Sandstrom et al. 2012). The spatially resolved maps are produced by stepping the IRS slit perpendicular and parallel to the source in steps of half a slit width for the LL module (5.″08) and the full slit width for the SL module (3.″7). The LL maps for N76 had 75×6 steps ($376'' \times 395''$) with a 14 s integration time per position. The SL maps are created similarly, except the steps are using the full slit width in order to increase coverage and have 120×5 steps ($220'' \times 208''$).

Each set of LL and SL observations has an associated background observation taken at R.A. $1^h9^m40^s$ decl. $-73°31'30''$ (J2000), a region chosen from the Multiband Imaging Photometer for Spitzer (MIPS) and Infrared Array Camera (IRAC) observations of the SMC to have negligible emission from the SMC itself (Bolatto et al. 2007; Leroy et al. 2007; Sandstrom et al. 2010). We subtract the background from the basic calibrated data files, which removes emission from the zodiacal light of the Milky Way cirrus, and reduces the number of "hot" pixels that contaminate the IRS data.

2.1.1. Constructing the Data Cubes

The basic calibrated data files are assembled into cubes using the software CUBISM (Smith et al. 2007a, we use version 1.8). CUBISM processes the 2D slit spectral images created by scanning the IRS slit across the source into 3D spectral data cubes through polygon-clipping-based reprojection. This algorithm is flux-conserving and is specially adapted for the IRS on Spitzer. We apply a slit-loss correction for extended sources which assumes uniform extended emission inside and outside the slits and corrects the native tuning of the IRS pipeline that assumes point sources. The IRS is susceptible to hot, "rogue," or bad pixels that appear on the cube images as repeating stripes, resulting from the bad pixel scanning across the image through the grid of positions. These pixels are often caused by interactions between the IRS CCD and solar wind particles. The positions and intensity of the rogue bad pixels can vary on scales of hours to days, making them unpredictable. Some bad pixels can be flagged automatically through CUBISM, but many must be flagged by hand. We perform extensive flagging of the bad pixels in each data cube ($\sim 7\%$ of data), with a

particular focus on the emission from the spectral lines we plan to model, in order to produce the cleanest spectral line maps.

2.1.2. Fitting Spectral Line Maps

We use the program PAHFIT (Smith et al. 2007b) to create line maps for each emission line in the IRS bandpass. PAHFIT uses a physically motivated model to simultaneously fit multiple components in an IRS spectrum. Its model includes dust continuum in fixed equilibrium temperature bins, starlight, bright emission lines, individual and blended PAH features, and extinction from silicate grains. In our fits, we do not include extinction because the SMC has very low levels of mid-infrared dust absorption, due to its relatively low gas-to-dust ratio (Lee et al. 2009; Roman-Duval et al. 2014). The mapping strategy produces maps for both the SL and LL modules, but the placement of the apertures corresponding to each spectral order creates an offset of the mapping area between the different modules and orders, resulting in different coverage for SL1, SL2, LL1, and LL2 (see Figure 3 in Sandstrom et al. 2012, for an illustration of the coverage on N 76). To maximize the area of the line maps, we fit each IRS module and spectral order separately with PAHFIT.

In order to create the emission line map, we first extract the spectrum for each pixel in the data cube. The native pixel size for the LL cubes is 5.″07, which is smaller than the point-spread function (PSF) at the lowest wavelength line ([S III] 18 μm, PSF FWHM of 4.″15) and highest wavelength ([Si II], PSF FWHM of 7.″61). The SL native pixel scale is 1.″85, which samples the PSF of the lowest wavelength line ([S IV], PSF FWHM of 2.″40) and the highest wavelength line ([Ne II], PSF FWHM of 2.″83). We pass the spectrum into PAHFIT with a custom emission line fitting list to ensure the fainter lines not included in the default fitting list are incorporated. Then we extract the result of the line fit and construct the resulting line map using the fits for the individual pixels. The line maps of all emission lines (excluding PAHs and quadrupole H_2 transitions) found in N76 are presented in Figure 1. The integrated spectrum of N76 is presented in Figure 2.

In addition to the N76 nebula, the IRS maps also include emission from a well-studied nearby core-collapse supernova remnant SNR E0102-72 (Hayashi et al. 1994; Blair et al. 2000; Chevalier 2005). The focus of this work is on N76, so we refer the reader to Sandstrom et al. (2009) which investigates the mid-infrared properties of SNR E0102-72 in detail with the Spitzer IRS data set also used in this work. The supernova remnant (SNR) is masked out for all analyses in this paper.

2.2. Herschel PACS Observations and Spectral Line Images

In addition to the Spitzer IRS data, we also report far-infrared observations from the Herschel Photodetector Array Camera and Spectrometer (PACS) project 1431 (PI: R. Indebetouw). We downloaded the data from the ESA Herschel Science Archive and used the level 2 pipeline reduced data, which contains spectral data cubes of the [C II] 158 μm, [O I] 63 μm, and [O III] 88 μm lines. To produce the spectral line maps, we fit a polynomial of order one to the baseline, remove the continuum, and integrate over the spectral line. This process was repeated pixel-by-pixel over the full data cube to produce a line intensity image for [C II], [O I], and [O III]. Lastly, we convert to the same surface brightness units 10^{-8} W m^{-2} sr^{-1} used with the IRS. We compared this reduction to an independent reduction using the procedure in Cormier et al. (2015) and found an excellent agreement within the uncertainties (private communication, D. Cormier).

2.3. Estimation of Uncertainty in Emission Line Surface Brightness

For the Spitzer IRS data, CUBISM provides an uncertainty cube that corresponds to the statistical uncertainty of the IRS measurement. These uncertainties are then propagated into the PAHFIT code, where they are used for the chi-squared minimization fitting. The resulting uncertainty from the PAHFIT output is propagated into our emission line images. These estimates of the uncertainties, however, are lower limits since they only include noise from the detector readout and do not comprise any systematic errors such as uncertainties in the absolute calibration or the effective PSF due to perpendicular slit offsets in the map.

For the Herschel PACS data, we compute the rms noise outside of the signal integration per pixel as a 1σ statistical uncertainty for each channel. We then propagate the channel rms to calculate an uncertainty for the integrated signal. This process is repeated per pixel to create a map of the statistical uncertainties for [C II], [O I], and [O III].

In addition to the statistical uncertainties, we also calculate a "background" level for each emission line. We concentrate on modeling the emission from the HII region created by the WR/O-star binary ionization source AB7. There are other ionization sources across the SMC that can produce diffuse ionized gas throughout the galaxy (e.g., Haffner et al. 2009). In order to quantify and remove this extraneous emission, we identify a blank part of the map that is not contaminated by emission from the HII region (typically $\sim$80 pc away from AB7). We calculate the median surface brightness in this patch of sky and consider it the "background" for the given emission line. The background is very low, typically $\lesssim$5% of the emission line intensity. The background levels are generated for the IRS maps only because the PACS field of view only covers the N76 nebula and there are no regions in the PACS maps that would not be contaminated by N76.

2.4. PSF Matching

The spatial resolution of the Spitzer IRS changes as a function of wavelength as the telescope is diffraction limited, with a PSF FWHM ranging from 7.″6 at 34.8 μm for [Si II] to 2.″4 at 10.5 μm for [S IV]. In order to properly model the spectra, we need to convolve the spectral line images to a common PSF (e.g., Sandstrom et al. 2009; Smith et al. 2009). We follow the procedure described by Aniano et al. (2011) to create custom convolution kernels that will transform an image with a narrower PSF to a broader PSF. We refer the reader to Section A for a detailed description of the PSF matching.

2.5. Radial Profiles

The spatial information given by the resolved infrared emission lines helps differentiate between photoionization models. `Cloudy` simulates HII regions with a 1D radiative transfer code but can accommodate a variety of HII region geometries with the assumptions in a given model. Due to the spherical nature of N76 (see Figure 1), we use the spherical geometry in `Cloudy` to best match the observations. In order to properly compare with the models, we average the spectral

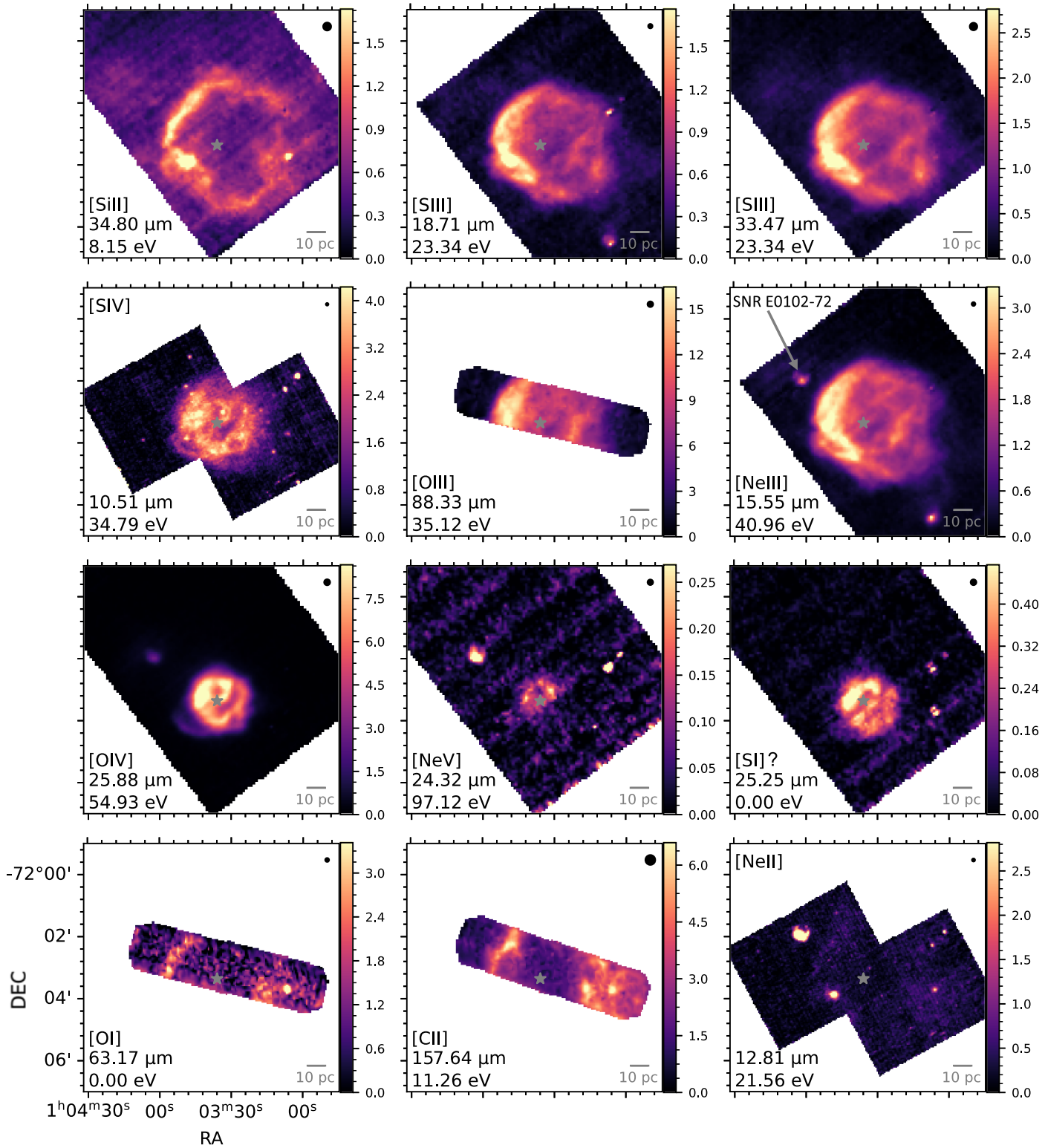

Figure 1. Images of infrared line emission in N76 where the color scale corresponds to the line brightness in 10^{-8} W m^{-2} sr^{-1}. The location of the WR-O star binary AB7, the ionization source of N76, is illustrated by a gray star in the center of each image. The supernova remnant (SNR) E0102-72 is located NE, on the upper left of N76, and is seen in some of the emission lines ([O IV], [Ne V], [Ne III], [Ne II]). The FWHM of the point-spread function (PSF) is shown in the upper right corner of each panel, and the ionization potential of the ion is displayed in the lower left corner together with the wavelength of each transition. These images show how the structure of N76 changes depending on the ion.

line images to create surface brightness radial profiles. N76 is an ideal region for this method because it is approximately spherically symmetric and mostly isolated from other bright regions (see Figure 1). We use the location of AB7 as the center of N76 and compute an azimuthal average with a radial bin size corresponding to one pixel or 5″. The radial profiles show how the line emission varies with distance away from the ionization source, thereby preserving some of the spatial information from

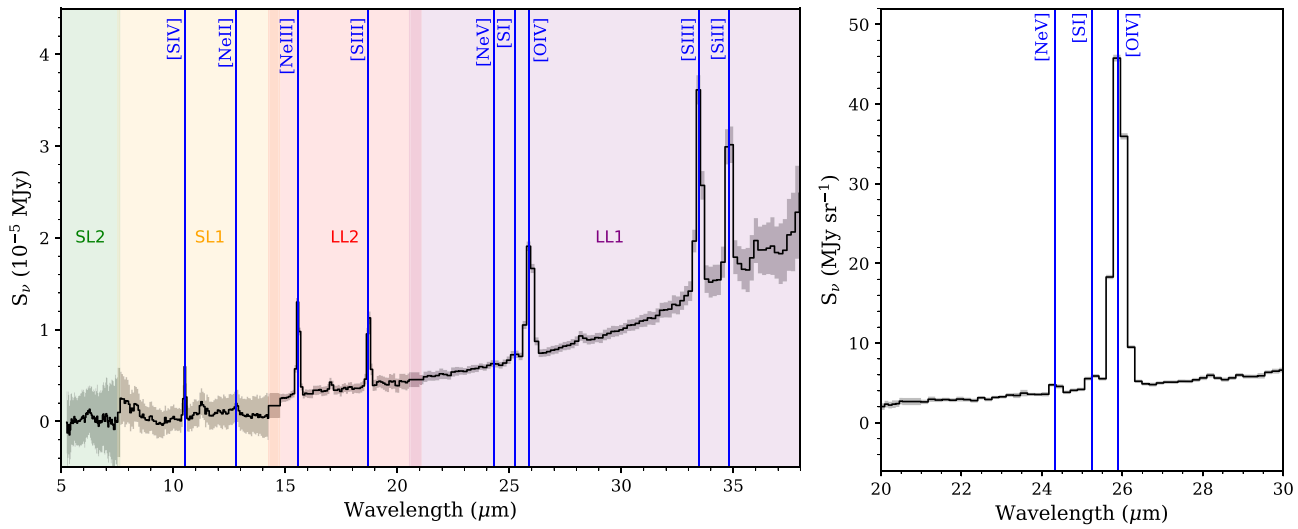

Figure 2. Left: integrated spectrum of the N76 region showing the ionized gas lines in N76 we model with Cloudy. Line labels are in blue and the orders of the IRS instrument are presented through the background color. Right: spectrum at a single line of sight toward the location of the WR binary AB7 that highlights the [Ne V] and possible [S I] features.

the spectral line images but making it simple to compare to properly integrated 1D Cloudy models. The radial profiles measured for each line are presented in Figure 3, showing that higher ionization lines generally peak closer to AB7. We also report the standard deviation in a given azimuthal bin as the gray uncertainty bars in the profile.

2.6. Integrated Intensities

In addition to examining the resolved surface brightness of the infrared emission lines through radial profiles (Section 2.5), we also record the total intensities by integrating across the nebula for the emission lines from Spitzer IRS. We aim to compare the observed total intensity of N76 for each line to the predictions of the total intensity from Cloudy as a secondary check of the models. The lines from Herschel PACS ([C II], [O I], and [O III]), however, only cover a strip of the N76 nebula and not correcting for this missing area and flux leads to underpredictions of the total intensity of N76. We identify the missing area for each PACS line by using the Spitzer IRS emission line that has the most similar radial profile. For [C II] and [O I] we use [Si II], and for [O III] we use [Ne III]. To correct for the missing flux, we multiply the flux contained in the PACS footprint by the ratio of the total area of N76 for that emission line to the area of the PACS footprint. We note that this modified version of the PACS maps is only used for the integrated total intensities reported in Table 1 and is not used for the radial profiles. The uncertainties in the integrated intensities are derived from the statistical uncertainties propagated through the total intensity calculation (see Section 2.3). The integrated intensities for all the emission lines are reported in Table 1.

2.7. [O IV] and [Fe II] Line Blend

The spectral resolution of $R\sim70$ in the Spitzer IRS LL module causes the [O IV] 25.89 μm and [Fe II] 25.99 μm lines to be blended. For this work, we assume that the flux of the line observed at 25.9 μm is dominated by [O IV] emission. The Cloudy models are tuned to the parameters of the AB7 system determined from modeling the optical and UV spectra in Shenar et al. (2016; see Section 3) and find that [O IV] 25.89 μm emission is 2 orders of magnitude brighter than [Fe II] 25.99μm line, strongly indicating that [Fe II] makes a negligible contribution to the 25.9 μm. The Cloudy models are inconsistent with a large contribution of [Fe II] to the 25.9 μm blend due to the nature of the hot WR star as the ionization source. Further, the resolved images of N76 show that the emission at 25.9 μm is centrally concentrated and associated with the high ionization zone of the HII region, making it much more likely to be a line with an ionization potential of 55 eV ([O IV]) rather than 7.9 eV ([Fe II]). There are also no detections of the iron lines at [Fe II] 17.94 μm or [Fe III] 22.93 μm in N76. Baldovin-Saavedra et al. (2011) use the high-resolution Spitzer module (LH), which can resolve the 25.9 μm [O IV] and [Fe II] blend. In their observations of the Taurus Molecular Cloud, they find that the [Fe II] 25.99 μm line is a factor of 3 brighter than [Fe II] 17.94 μm, consistent with theoretical predictions in Hollenbach & McKee (1989). Using this relationship, we calculate an upper limit of the [Fe II] 25.99 μm in N76 of 1.3×10^{-10} W m^{-2} sr^{-1}, which would imply <5% of the 25.9 μm line surface brightness comes from [Fe II] 25.99 μm emission. Therefore, [Fe II] contributes a negligible component of the 25.9 μm line and we will assume for this work that the line flux is dominated by the [O IV] line. The [O IV] line dominating the 25.9 μm blend is also consistent with observations of blue compact dwarf (BCD) galaxies, which have similar metallicities and ionization parameters as N76 (Hunt et al. 2010).

3. Photoionization Models

3.1. Cloudy Model Parameters

We use version C17.01 of Cloudy (Ferland et al. 2017) to model the properties of the ionized gas in N76. Cloudy is a spectral synthesis code designed to simulate physical conditions and the resulting spectrum from gas and dust that is exposed to an ionizing radiation field. In order to produce a model, a variety of input parameters are required as listed below.

Ionizing source SED: The shape of the source spectrum as a function of photon energy must be specified in Cloudy, which for N76 corresponds to the spectral energy distribution (SED)

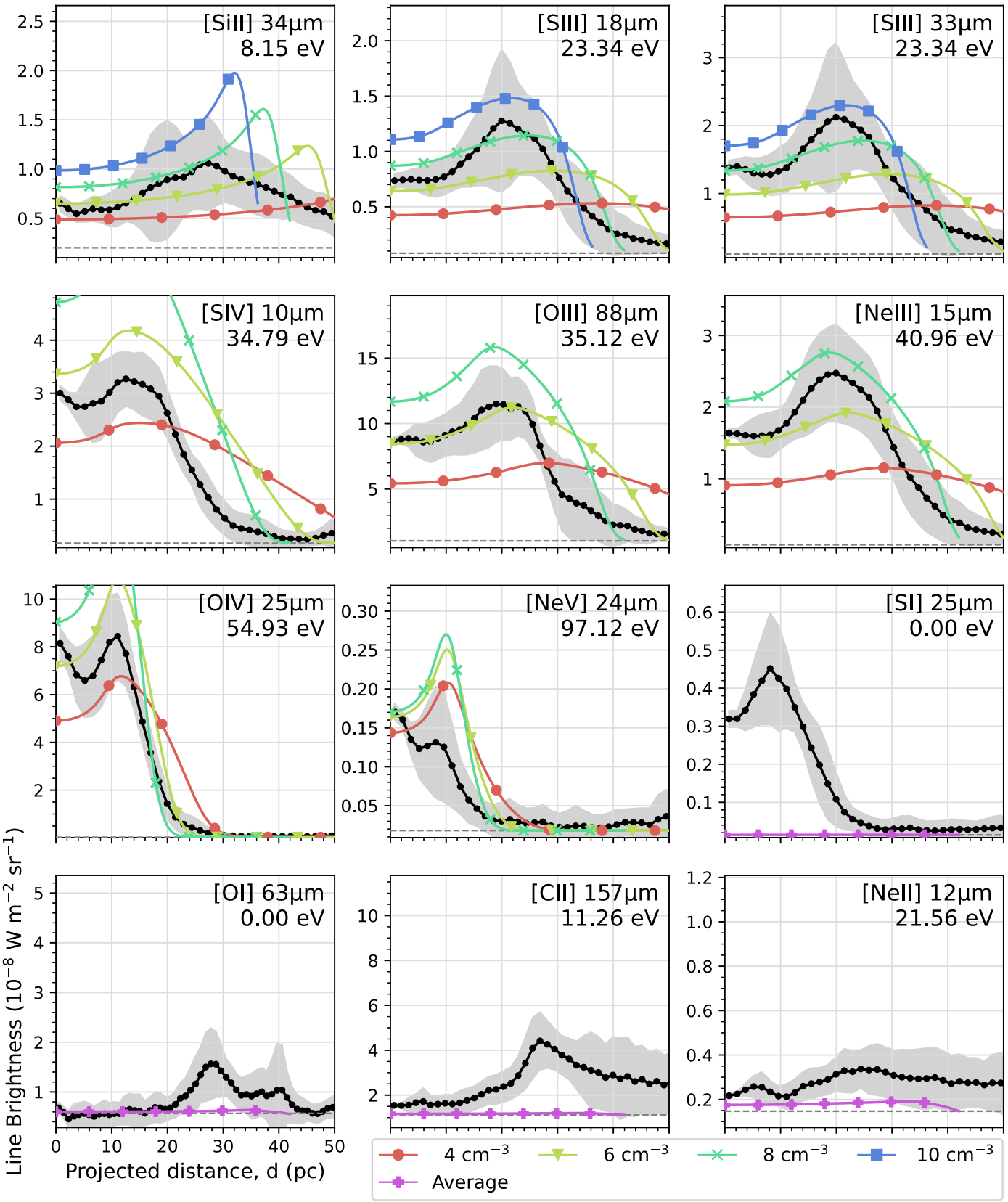

Figure 3. Radial profiles of observed emission line brightness and `Cloudy` photoionization models. The black circles represent the average line brightness of a given emission line as a function of distance away from AB7, the gray region is the standard deviation in a given bin, and the dashed line represents the background diffuse contribution to the emission line (see Section 2.3). The `Cloudy` models vary with hydrogen density and are represented by the colored lines and symbols, with the average of all models presented in purple crosses. The ions that originate from the photoionized gas (excluding emission lines that can be produced through neutral material ([C II] and [O I]) see Section 4.4, or the diffuse ionized gas, Section 4.5) are well predicted by the `Cloudy` models that range in density from $n_{\rm H} \sim 4$ cm^{-3}–10 cm^{-3}. Both the surface brightness and the shape of the radial profiles are well predicted in these cases.

Table 1
Line Properties and Intensities

Line	λ (μm)	Ionization Potential (eV)	n_{crit} (cm^{-3})	FWHM (arcsec)	Instrument	I_{obs} (10^{-15} W m^{-2})		I_{cloudy} (10^{-15} W m^{-2})	
						Total	Orig	$n_H = 4$ cm^{-3}	$n_H = 10$ cm^{-3}
[SiII]	34.80	8.2	2×10^3	7.61	LL1	14.75 ± 0.01	…	17.16	14.37
[SIII]	18.71	23.3	2×10^4	4.15	LL2	11.28 ± 0.73	…	13.00	12.49
[SIII]	33.47	23.3	7×10^3	7.17	LL1	18.93 ± 0.00	…	20.57	19.52
[SIV]	10.51	34.8	5×10^4	2.40	SL1	17.58 ± 2.35	…	35.05	41.65
[OIII]	88.33	35.1	5×10^2	5.35	PACS	111.68 ± 2.25	50.21 ± 1.01	138.40	143.00
[NeIII]	15.55	41.0	3×10^5	3.51	LL2	22.05 ± 0.70	…	28.33	28.67
[SI]	25.25	0.0	1×10^5	5.44	LL1	1.04 ± 0.14	…	0.00	0.00
[OI]	63.17	0.0	9×10^5	3.63	PACS	15.74 ± 3.37	4.49 ± 0.90	1.30	1.02
[CII]	157.64	11.3	5×10^1	9.43	PACS	60.35 ± 1.20	16.70 ± 0.33	1.95	1.31
[NeII]	12.81	21.6	7×10^5	2.83	SL1	4.52 ± 1.70	…	0.92	0.71
[OIV]	25.88	54.9	1×10^4	5.66	LL1	20.35 ± 0.04	…	28.99	29.38
[NeV]	24.32	97.1	1×10^5	5.22	LL1	0.20 ± 0.06	…	0.49	0.37

Note. Description of the spectral lines modeled, including the integrated intensities measured and the predicted integrated intensities with two densities from Cloudy. The Ionization Potential is the photon energy required to produce the observed ionization state from the lower ionization state. The critical density is for collisions with electrons. The lines observed with Herschel/PACS, and given as I_{obs} Orig, do not cover the full nebula (see Figure 1); I_{obs} Total contains the total intensity corrected for this missing flux.

of the central binary. We use SED models in Shenar et al. (2016) that constrain the stellar parameters of AB7 binary through a combination of UV spectroscopy from the International Ultraviolet Explorer (IUE) and the Far Ultraviolet Spectroscopic Explorer (FUSE) as well as optical spectroscopy taken from Foellmi et al. (2003). The stellar parameters of the WR and its O star companion were identified by matching the observed spectra to models from the non-LTE Potsdam WR (PoWR) model atmosphere code[8] (Gräfener et al. 2002; Hamann & Gräfener 2003, 2004; Sander et al. 2015; Hainich et al. 2019). These PoWR models are set to use the SMC metallicity and derive a variety of parameters for the WR and O stars. Shenar et al. (2016) report that the WR is a WN4 spectral type with a temperature of $T_* = 105{,}000$K, wind speed of $v_\infty = 1{,}700$ km s^{-1}, surface gravity of log $g_* = 4.7$ cm s^{-2}, a low ($X_H \approx 0.15$) hydrogen fraction, a transformed radius of $\log R_t = 0.75\, R_\odot$, and a mass-loss rate of log $\dot{M} = -5.0\, M_\odot$ yr^{-1} . The O star companion is classified as an O6 I(f) star and has a temperature of $T_* = 36$ kK, wind speed of $v_\infty = 1{,}500$ km s^{-1}, surface gravity of log g=3.6 cm s^{-2}, and a mass-loss rate of log $\dot{M} = -7.0\, M_\odot\, yr^{-1}$.

The PoWR models are normalized by default to a luminosity of $L_\odot = 5.3\, L_\odot$. Therefore, we scale the SEDs fitted in Shenar et al. (2016) by their luminosities of log $L_\odot = 6.1$ for the WN4 and log $L_\odot = 5.5$ for the O6 components. We then add the luminosity-weighted WN and O6 SEDs together to produce a total SED for the AB7 binary system, shown in Figure 4. The feature at 40 eV in the spectrum is due to a strong FeV emission line at 305.31 Å.

Elemental abundances: Instead of scaling gas-phase Milky Way abundances to the metallicity of SMC, we employ the best gas-phase abundances available for SMC HII regions. Relative abundances of elements are different in the Magellanic Clouds and the Milky Way due to different nucleosynthesis histories (Russell & Dopita 1992). For the majority of elements, we adopt the abundances given for HII regions provided in Dufour (1984) and Russell & Dopita (1992), but we slightly modify the abundances for sulfur and silicon to best match the observations in N76 (see below). Our adopted abundances and the references used are in Table 2.

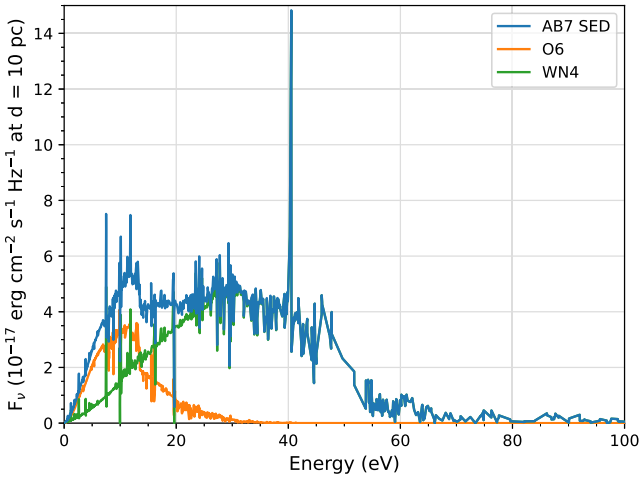

Figure 4. The SED of the AB7 system for `Cloudy` input. We use the Potsdam Wolf–Rayet database models for the WN Wolf–Rayet (Hamann & Gräfener 2004; Todt et al. 2015) and O6 (Hainich et al. 2019) stars in the AB7 binary and combine them into one input SED. The full SED for AB7 is in blue, the WR is green, and the O star is orange.

We decrease the sulfur abundance by a factor of 2 from the $(S/H) = 3.9 \times 10^{-6}$ value reported in Russell & Dopita (1992). Without this modification, the three sulfur lines observed in this work ([S III] 18 μm, [S III] 33 μm, and [S IV] at 10 μm) are consistently overpredicted by a factor of 2 in our Cloudy models. This small variation in the sulfur abundance is also consistent with the scatter presented in Russell & Dopita (1990), the value of $(S/H) = 1.8 \times 10^{-6}$ reported in Dennefeld & Stasińska (1983), and the sulfur abundances found in Vermeij & van der Hulst (2002) and Lebouteiller et al. (2008) that use infrared data.

Identifying an abundance of silicon is more complex because silicon is often depleted in dust. While the dust abundance is often lower in HII regions than in HI regions or molecular clouds, dust can still be present and have an impact on HII regions, especially toward the outer edges where the ionized

[8] www.astro.physik.uni-potsdam.de/PoWR.html

Table 2
Adopted SMC Abundances

Element	Abundance (X/H)	Reference
He	8.13×10^{-2}	2
C	1.45×10^{-5}	1
N	4.27×10^{-6}	2
O	1.07×10^{-4}	2
Ne	1.86×10^{-5}	2
Al	2.51×10^{-6}	2
Si	4.88×10^{-6}	3,4
S	1.95×10^{-6}	2

Note. References are (1) Dufour (1984), (2) Russell & Dopita (1992), (3) Tchernyshyov et al. (2015), and (4) Jenkins & Wallerstein (2017).

hydrogen fraction is lower and the [Si II] emission is brightest. Russell & Dopita (1992) provide only a photospheric abundance for silicon that does not take into account the depletion from dust. We therefore use elemental depletion studies in the SMC to calculate the median gas-phase abundance for silicon (Tchernyshyov et al. 2015; Jenkins & Wallerstein 2017). The median silicon depletion from these studies is 0.4 which happens to accurately match the observed flux of [Si II]. We note that this systematic uncertainty in the silicon HII region abundance leads to an uncertainty in the prediction for the [Si II] flux (see discussion in Section 4.4).

Stopping criteria: We are interested in modeling the ionized gas properties of N76 and therefore will run the `Cloudy model` to the end of the ionization zone at the transition between the HII region and photodissociation region (PDR). We therefore define the H II region end to be the point at which the PDR begins and the gas is neutral. The focus of this work is to model the ionized gas so continuing the model into the PDR is unnecessary, but has the consequences of underestimating the emission from the neutral-dominated lines [Si II], [C II], and [O I] (see Section 4.4). After using a range of stopping conditions we find that an electron temperature cutoff of 2000 K accurately probes the ionized gas to the end of the ionization front.

Geometry: We assume a spherical geometry to approximate the geometry of N76. The sphere command in `Cloudy` sets the geometry to be closed and assumes that the gas fully covers the ionization source.

Inner radius: The inner radius is defined as the distance between the gas and the ionization source. The massive, fast stellar winds produced by WR stars often form a stellar wind-blown bubble (SWB) structure in the resulting nebula (e.g., Weaver et al. 1977). As we discuss in Section 4.3, the region closest to AB7 has been shocked by the stellar winds and is occupied by this tenuous very hot plasma. For the purposes of our modeling, this effect is best reproduced by a central cavity in the gas. We vary the gas inner radius and find a radius of 10 pc to best reproduce the observed emission line radial profiles.

Hydrogen density: The density input in `Cloudy` is the total hydrogen density. We assume the density of the HII region is constant, a reasonable assumption for classical, spherical HII regions, and the density remains constant up to the ionization front of the region. We produce multiple constant density models that vary from $n_H = 1$–$50\,cm^{-3}$ in order to best constrain the density in N76 with the observed emission lines.

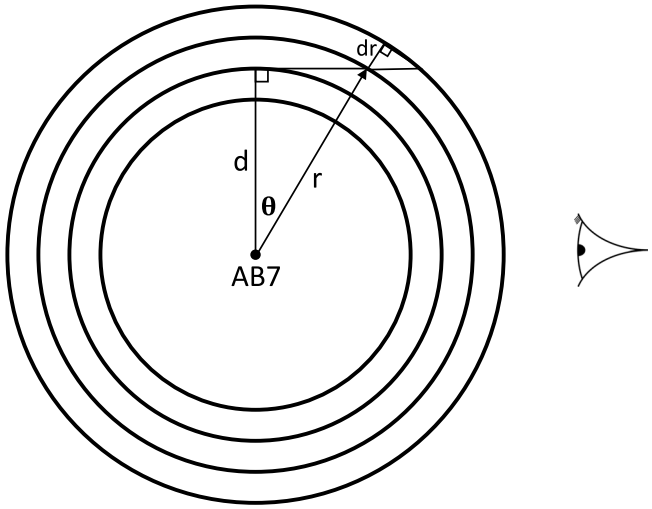

Figure 5. Schematic showing the geometry of calculating the projected intensity from `Cloudy` models where d is the projected distance, r is the physical distance, and dr is the differential distance between shells. The observer is peering from the right of the figure.

The range of hydrogen densities between $n_H = 4$–$10\,cm^{-3}$ that fit the data best are presented in this work.

Since the binary at the center of N76 is well-studied, most of the inputs in the `Cloudy` model use a priori knowledge of the ionization source, abundances, and geometry.

3.2. Calculating Predicted Radial Profiles

N76 is an approximately spherical shell, also known as a bubble nebula, with a radius of about 40 pc. Because of the approximately symmetric nature of the nebula, we compare the `Cloudy` models and the observations using radial profiles. `Cloudy` models report the volume emissivity of each transition as a function of depth into the nebula. In other words, they provide the radial profile of emissivity in a sphere. To compare with the observations, we need to appropriately project these profiles to compute the azimuthal average surface brightness as a function of the projected distance from AB7 for each of the emission lines. A point that is at a distance d from the source in projection has contributions from shells that have radii between d and infinity in proportion to their emissivity and projected thickness. Figure 5 shows the geometry of the N76 `Cloudy` model and the relationship between different shells, the projected distance d, and the physical distance r. The projected surface brightness for the `Cloudy` model then is:

$$I(d) = \frac{1}{2\pi}\int_d^\infty \frac{\epsilon(r)}{\sin\theta} dr, \quad (1)$$

where r is the physical 3D distance from AB7, $\epsilon(r)$ is the radial dependence of the line volume emissivity reported from `Cloudy`, d is projected distance from AB7, and θ is the angle between d and r. We convert Equation (1) to eliminate θ resulting in

$$I(d) = \frac{1}{2\pi}\int_d^\infty \frac{\epsilon(r)}{\sqrt{1 - d^2/r^2}} dr, \quad (2)$$

and calculate the surface brightness predicted from the `Cloudy` model, $I(d)$, as a function of the projected distance and volume emissivity reported from `Cloudy` in order to compare to the observed data. We set the `filling factor`

in Cloudy to unity to reflect that the resolved emission in N76 is not clumpy.

The Cloudy models use AB7 as the only ionization source, but there may be contributions of low ionization ionized gas from the warm ionized medium to our observed emission lines (e.g., Haffner et al. 2009). To account for this, we add the constant surface brightness background value calculated in Section 2.3 to the radial profiles derived from the Cloudy models. This background is typically very low representing $\lesssim$5% of the total surface brightness. Lastly, the final Cloudy profiles are convolved with a Gaussian kernel with an FWHM of 12″ to make an equal comparison to the 12″ PSF-matched emission line images.

4. Results

4.1. Comparison of Models to Observations

Figure 3 shows the results of the constant density Cloudy model with hydrogen densities $n_{\rm H} = 4$–10 cm^{-3}. We compare the models projected on the plane of the sky (Section 3.2) with the measured emission line radial profiles (Section 2.5). Therefore, we compare not only the integrated intensity of the emission line, but also how well its predicted distribution matches the data. The emission lines we sample are at a variety of ionization energies and therefore trace the different ionization zones in the nebula. For example, the [O IV] line ($E_{\rm ion} = 55$ eV) peaks at 10 pc while the [S III] line ($E_{\rm ion} = 23$ eV) peaks at 20 pc. A model that predicts an emission line well will have a similar peak, spatial gradient, and ending position as the observed radial profile

There is not a single constant density model that is able to predict the shape and intensity of all of the emission lines, but most emission lines are consistent with a given constant density model in the range of $n_{\rm H} = 4$ cm^{-3} to $n_{\rm H} = 10$ cm^{-3}. In some cases, the spatial distribution of the profile is better matched by a model that does not predict the intensity as well. For example, in the [S IV] profile, the 8 cm^{-3} model predicts the shape very well but is about 50% more luminous than the observations. These small discrepancies are likely due to our constant density and spherical symmetry simplifying assumptions. While there are small differences between the models and observed emission line profiles, overall Cloudy predicts the emission from ionized gas very well with simple models in a narrow density range, except for a few transitions that we will discuss in detail.

In addition to the projected surface brightness profiles from the Cloudy models, we also report the predicted total intensities in the Cloudy models in Table 1 for the 4 cm^{-3} and 10 cm^{-3} models. Overall the radial profiles of the surface brightness provide a much more precise way of differentiating between the constant density Cloudy models than examining the integrated intensity. For example, the integrated intensity of [Ne III] varies between the 4 cm^{-3} and 10 cm^{-3} models by 28.33–29.38 W m^{-2}, a <1% difference. In contrast, the radial profile of the 4 cm^{-3} model peaks 10 pc after the 10 cm^{-3} does, clearly showing it does not match the spatial distribution of the [Ne III] emission. Thus a comparison between the spatially resolved radial profiles provides much more information than using just integrated intensities.

To produce both the Cloudy models and the measured radial profiles we assume that N76 is spherically symmetric with AB7 in the center of the nebula. This is approximately true, but not precisely correct. Figure 1 shows that AB7 appears offset in the eastern direction. Additionally, there is an overall trend for the ionized gas lines to be much brighter on the eastern edge of the nebula in comparison to some of the neutral gas lines ([CII] especially) that have brighter emission on the western edge. We explore the effects of the asymmetries on our results in Appendix B. Images of the $H_2S(1)$ transition and ancillary ALMA CO data (Figure 7) confirm that there is a molecular cloud complex on the western side of N76. Therefore, there are likely internal density gradients as well as a wall of dense gas on the western side of the nebula breaking the symmetry assumption. For example, because AB7 is slightly offset from the center, the radial averaging produces flatter slopes with respect to the models. We have attempted to account for some of this offset by showing the profiles as a strip instead of radially in Appendix B. These show the structure on the different sides of the nebula and how a particular density is a better predictor for one side compared to the other.

We also report the ionization structure predicted by Cloudy of each element in Figure 6 to complement the projected profiles of surface brightness. The panels show the ionization state of the relevant elements as a function of the physical distance from AB7. In addition to the ions that are studied in this paper, we also plot the ionization structure of helium. As the most abundant element after hydrogen, helium can have a significant impact on the ionization equilibrium of HII regions. This impact is most pronounced in HII regions illuminated by hard radiation fields, due to the fact that their central sources produce a lot of photons capable of ionizing and doubly ionizing helium: the ionization potentials of He^0 and He^+ are 24.6 eV and 54.4 eV respectively. Ionization cross sections are sharply peaked at the ionization energy: the cross section of He^0 to 24.6 eV photons is 10 times higher than that of H^0, therefore these photons will preferentially ionize helium over hydrogen. For sources with a hard enough spectrum, characterized by the ratio of the rate of production of He-ionizing photons (Q_1) to H-ionizing photons (Q_0), this can lead to the He^+ region extending slightly past the H^+ region. In fact, $Q_1/Q_0 \sim 0.15$ is needed for the HII and HeII regions to be equivalent sizes (Draine 2011), while for N76 the $Q_1/Q_0 \sim 0.55$ calculated from the Cloudy models matches the slightly larger HeII emitting region seen in Nazé et al. (2003). A similar effect is seen in the ionization structure of neon, where the [Ne II] emission extends slightly past the hydrogen ionization front.

4.2. The High Ionization Lines: [Ne V] and [O IV]

The high ionization lines, [Ne V] and [O IV], with ionization potentials of 97 eV and 55 eV, respectively, can often be difficult to reproduce through just photoionization from O and B stars. Models of hot, low-metallicity WR stars around ages of 3–4 Myr like the WR in AB7, however, contain enough high-energy photons to have Ne^{+4} and O^{+3} ions and produce appreciable [Ne V] 24 μm and [O IV] 25 μm emission (Schaerer & Vacca 1998; Schaerer & Stasińska 1999). The N76 photoionization models presented here are able to accurately predict both the flux of the [Ne V] and [O IV] lines (see Table 1) as well as their spatial distribution (see Figure 3). The [Ne V] is slightly overpredicted by the Cloudy models by a factor of 2, which can be explained by density variation (either through clumping or a lower density in the high ionization zone) or uncertainty in the PoWR model (see below).

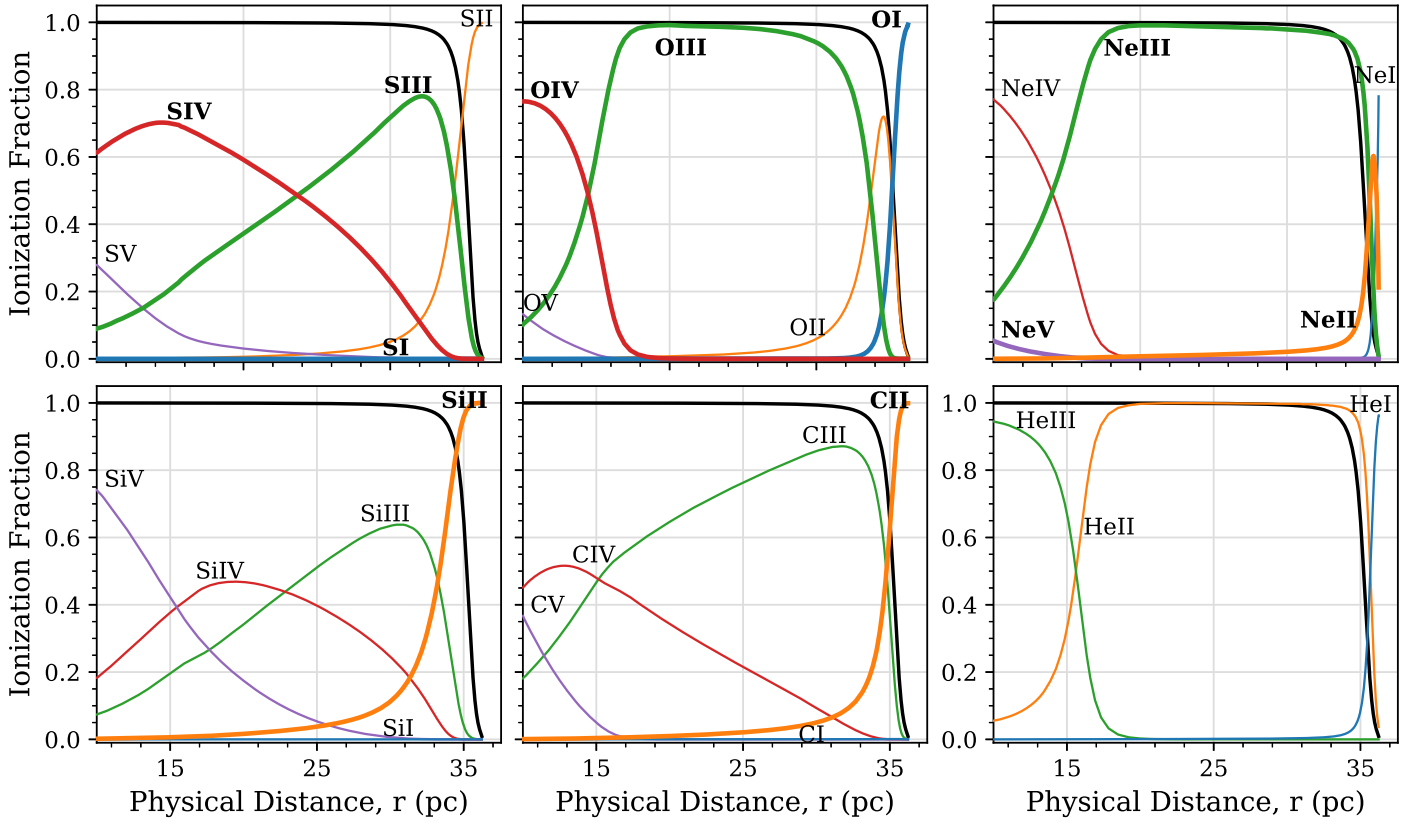

Figure 6. The ionization structure of sulfur, oxygen, neon, silicon, carbon, and helium from the 10 cm^{-3} constant density `Cloudy` model beginning at the photoionized region (r = 10 pc). Ions that are presented in this paper are bold, and we also show the structure of ionized hydrogen in black. The various ionization zones can be seen throughout these elements in physical distance, similar to the projected distance seen in Figure 1.

We note that the predicted flux of the [Ne V] and [O IV] lines are highly dependent on small changes to the PoWR model that impact the high-energy (55+ eV) tail of the SED. A `Cloudy` model using a PoWR SED with the same input parameters but increasing the hydrogen fraction from $X_H \sim 0.15$ to $X_H \sim 0.2$ produced no [Ne V] emission and a fraction (<10%) of the observed [O IV] emission. Additionally, the O star companion to the WR in AB7 contains a small X-ray contribution to the SED, implied by the presence of OVI in its spectrum, but contributes a negligible (<5%) amount to the [O IV] and [Ne V] flux (see Shenar et al. 2016 for more details).

Further, Nazé et al. (2003) report narrowband optical imaging of N76 and find bright HeII 4686Å emission that is inconsistent with the hottest WR models at the time. The `Cloudy` models presented here, however, are able to reproduce the reported HeII emission within a factor of 2. The spatial distribution of the HeII emission (see Figure 4 in Nazé et al. 2003) is very similar to the [O IV] emission, likely due to their similar ionization potentials.

4.3. The Windblown Cavity

The `Cloudy` photoionization models require a 10 pc cavity to reproduce the observed spatial distribution of the ionized gas lines. The origin of this cavity is from the stellar winds of the WR and O star in AB7 interacting, shocking, and heating the surrounding ISM, creating a stellar windblown bubble (SWB). The resulting nebula consists of an onion-like structure (see Figure 1 in Weaver et al. 1977; Freyer et al. 2003) with four layers, including (1) an innermost, free-flowing supersonic wind that travels into (2) a hot ($\sim 10^6$–10^8 K), shocked gas region that will expand into (3) the photoionized shell of swept up interstellar gas, and finally into (4) the ambient interstellar medium. The hot, shocked material in shell 2 is typically at much higher pressures than shell 3, and will expand as a function of time. Assuming a uniform-density spherical shell with equal pressure throughout and that the thermal energy contained within shell 2 is much higher than the kinetic energy, Weaver et al. (1977) derived a relationship between the radius of hot, shocked gas bubble (shell 2) as a function of time, such that

$$r_{s2}(t) = \left(\frac{125}{154\pi}\right)^{1/5} L_w^{1/5} \rho_0^{-1/5} t^{3/5} \text{ cm}, \quad (3)$$

where $\rho_0 = n_0 m_H$ is the density of the ambient medium in g cm^{-3}, $L_w = \frac{1}{2}\dot{M}_w v_w^2$ is the stellar wind luminosity in g cm^2 s^{-3} with $\dot{M}_w$ as the mass-loss rate and v_w as the terminal velocity of the stellar wind, and t is the time of expansion in seconds. We calculate the size of the bubble blown by the WR star in AB7 through the values characterized by Shenar et al. (2016), $\dot{M} = 10^{-5}$ $M_\odot$ yr^{-1}, $v_w = 1.7 \times 10^3$ km s^{-1}, and assume $n_0 = 10$ cm^{-3}. Using these parameters, a 10 pc radius bubble is created after 0.2 Myr of free expansion. This is consistent with the evolutionary tracks studied in Shenar et al. (2016), where they find an age of 3.4 Myr for the AB7 system and estimate the WR star has been in the WR stage for ~0.1–0.2 Myr.

Another contribution to the cavity in N76 may be through the colliding stellar winds from the WR and O stars. There is ample evidence of shocks originating from colliding wind systems, such as the winds produced by the WN4 and O6 stars

in AB7 (e.g., Stevens et al. 1992; Tuthill et al. 1999; Parkin & Pittard 2008). However, the spatial scale of the colliding wind zone is comparably insignificant to the size of the photoionized cavity, corresponding to $\sim 10^{-6}$ pc for AB7. Further, Chandra observations of AB7 show X-ray-emitting gas attributed to shocks from the colliding winds, but the region is only ~3.5 pc in radius (Guerrero & Chu 2008). Thus the SWB structure described in Weaver et al. (1977) likely creates the implied cavity in the presented photoionization models.

It is possible that shocks from either the colliding winds of the AB7 system or the stellar windblown bubble could contribute additional sources of [Ne V] and [O IV] in N76. We investigate this by calculating the velocity and postshock temperature needed to ionize Ne^{+3} into Ne^{+4}. We estimate a temperature of $T \sim E_{ion}/k_B \sim 10^6$ K by taking the ionization energy of [Ne V]. Using the relationship between the postshock temperature (Equation (36.28) of Draine 2011) and the shock velocity, we find the minimum velocity for the shock is $v \approx 290$ km s^{-1}. Toalá et al. (2017) study the WR nebula NGC 3199 in the Milky Way and find diffuse X-ray emission that corresponds to a plasma temperature of $T \approx 1.2 \times 10^6$ K, very similar to the temperature required to produce the [Ne V] emission observed in N76. Further, models of stellar wind-blown bubbles show velocities of ~200–400 km s^{-1}, enough to ionize Ne^{+3} into Ne^{+4} (Freyer et al. 2003, 2006; Lancaster et al. 2021). Since the Cloudy photoionization models already slightly overpredict the [Ne V] emission, it is unlikely there is this additional contribution from shocks. The cavity may contain ions of neon at much higher-energy states not detected by our current data set.

Fast, radiative shocks with velocities ~300–500 km s^{-1} can explain optical observations of [Ne V] and He II in low-metallicity, BCD galaxies (e.g., Thuan & Izotov 2005; Izotov et al. 2012, 2021). However, the origin of these shocks is typically attributed to supernovae (SN), not stellar winds. Indeed, the supernova remnant E0102-72 that serendipitously is in the N76 field is a bright [Ne V] source (see Figure 1), suggesting shocks from SN can produce appreciable [Ne V] emission. The SNR is too far away from N76 to contribute to the [Ne V] emission associated with the nebula (see Figure 1). Therefore, the [Ne V] within the N76 nebula is most likely produced through photoionization. We note that if N76 was placed at the larger distances of the BCD galaxies studied in Izotov et al. (2021), it would be difficult to differentiate between [Ne V] produced through the WR nebula and the SNR due to the lower physical resolutions.

4.4. The Neutral Gas-dominated Lines: [O I], [C II], and [Si II]

We define the neutral-dominated lines as ions or atoms that can come from neutral gas, i.e., those ions that have an ionization potential less than that of hydrogen. Most of these neutral-dominated emission lines are underpredicted by the Cloudy models because the Cloudy models were designed to model the ionized gas and do not probe farther than the ionization front after the transition from ionized to neutral material. Further, Figure 6 shows the ionization structure of carbon and oxygen, suggesting that the radiation field of AB7 is too hard for O^0 and C^+ to exist in the interior of the HII region where oxygen and carbon are in higher ionization states. Thus the bulk of emission from [O I] and [C II] comes from the neutral phases; future PDR modeling is needed to understand the nature of these neutral lines, which is beyond the scope of this study.

The fine-structure transition of silicon, [Si II], however, is reasonably well predicted by the Cloudy models. With an ionization potential of 8.15 eV for Si^0, [Si II] can come from the neutral gas. However, Cloudy modeling of the HII region reproduces both the total intensity and the surface brightness distribution of the [Si II] line (see Table 1 and Figure 3), unlike for the other neutral gas tracers. Figure 6 shows that the modeled abundance of Si^+ grows faster toward the edge of the HII region than that of C^+, which is consistent with the observed radial profiles presented in Figure 3. Thus the majority of the [Si II] emission is associated with the edge of the HII region, around the transition between ionized and atomic gas. In Section 5.1 we calculate the percentage [Si II] that comes from each phase.

Why are there dominant PDR contributions for [C II] and [O I] but not [Si II]? The [Si II] 34 μm fine-structure transition is at shorter wavelengths, and its excitation requires higher temperatures than [O I] 63 μm or [C II] 158 μm. Further, the [C II] and [O I] lines are also major coolants in the Warm and Cold Neutral Medium (Wolfire et al. 1995, 2003) and contributions from that can increase the total intensity of these lines by peering through the atomic gas in projection toward the SMC. In contrast, models presented in Wolfire et al. (1995, 2003) show the cooling from [Si II] in the atomic gas is 2 orders of magnitude lower than that from the [C II] and [O I] lines, which leads to a much fainter atomic gas contribution for the [Si II] emission. The intensity of the [Si II] emission is also highly dependent on the silicon gas abundance. Silicon is depleted heavily into dust, and in order to determine its gas-phase abundance we used depletion studies in the SMC (Tchernyshyov et al. 2015; Jenkins & Wallerstein 2017). The dust depletion of gas-phase silicon with respect to the photospheric abundances in the SMC (Russell & Dopita 1992) has a large range, factors from 1.25 to 0.05 (0.1 to −1.3 dex, our preferred abundance corresponds to 0.4, or −0.4 dex). The assumed silicon abundance matches well the observed radial profile in Figure 3. A lower silicon abundance leads to a [Si II] radial profile that does not match the overall shape and would suggest a larger fraction of [Si II] comes from the PDR. While we assume some silicon depletion in the ionized gas, our results suggest that even more silicon is depleted in the neutral phase, especially when compared to carbon or oxygen, which will decrease the available gas-phase silicon in order to produce the [Si II] emission. These combined effects likely explain the much smaller contribution of PDRs toward the observed [Si II] emission.

We present images of the other neutral gas tracers in N76 in Figure 7. The Spitzer IRS covers the quadrupole transitions of molecular hydrogen, H_2. Our PAHFIT pipeline simultaneously fits these lines and we show the brightest H_2 line, S(1) at 17 μm, in Figure 7. This line has $E/k \sim 1000$ K, traces H_2 at $T > 300$ K, and its presence indicates molecular material that is heated by a strong far-ultraviolet field or through shocks from the central WR star. We compare the H_2S(1) and [Si II] lines to the ACA CO(2–1) data presented in Tokuda et al. (2021). Interestingly, these neutral gas species are not always spatially coincident. As discussed above, the [Si II] emission originates mostly around the ionization front of the HII region and therefore traces the the outer shell of N76. The H_2 and CO

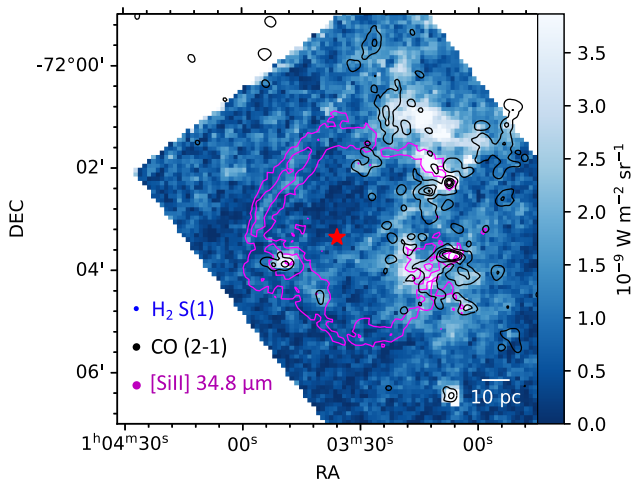

Figure 7. The neutral gas tracers in N76, with the $H_2S(1)$ quadrupole transition in the blue color scale, CO contours from Tokuda et al. (2021) in black (in levels of 1, 6, 11, 16 Jy beam^{-1}), and the [Si II] emission in magenta contours (in levels of 1, 1.5, and 3 $\times$ 10^{-8} W m^{-2} sr^{-1}). The beam/PSF size of each map is in the bottom left corner. The [Si II] emission primarily traces the outer shell of N76, suggesting [Si II] originates mostly from the transition between the ionized gas and the PDR. The CO and H_2 emission are brightest when AB7 illuminates the molecular ridge north and northwest of N76.

emission is brightest where AB7 illuminates the molecular ridge region that is north and northwest of N76.

4.5. Production of [Ne II] in N76

The Cloudy models predict a modest amount of [Ne II], about 20% of the observed [Ne II]. At an ionization potential of 21.56 eV, [Ne II] traces lower energy photons. Figure 6 shows how the ionization state of Neon transitions to Ne^+ at the very edge of N76 at a very small radius range compared to the higher ionization states and rapidly transitions into neutral Neon. Therefore, the total volume of the predicted [Ne II] emission from the Cloudy models is quite small, leading to a very weak predicted [Ne II] line. The excess of observed [Ne II] emission could be associated with other ionization sources besides AB7, such as smaller HII regions. It is also possible that [Ne II] traces the low-density, diffuse ionized gas at densities $n_e \lesssim 0.1\,\mathrm{cm}^{-3}$. In the nearby dwarf galaxy, IC 10, Polles et al. (2019) also find that their models underpredict the [Ne II] observations by a factor between three and four, suggesting that [Ne II] may be a tracer of the diffuse ionized gas in low-metallicity galaxies.

4.6. How Changes in the Model Affect the Inferred Conditions

Besides the density, for which we produce a grid of models, a variety of other Cloudy inputs can affect the final results of the modeling. The Cloudy models are most sensitive to the input luminosity and SED.

For example, decreasing the luminosity of the WR by 50% leads to a 56% reduction in the total intensity of the spectral lines at a constant density of $n_H = 10\,\mathrm{cm}^{-3}$. Naively, this reduction in the total intensity provides a slightly better fit for some lines, but it is at the cost of producing emission over a region with a smaller radius and a spectral line radial profile that does not match the data. Thus the strength of comparing the Cloudy models to the spatially resolved data shines through; using the a priori values for the spectrum and luminosity provides an overall better fit than if one were to directly match the total intensities.

We also experimented with using different stopping conditions, abundances, and the presence of dust. All of these parameters have a negligible impact on the overall results of the model, except for the abundances which we fixed in the manner described in Section 3.1 and Table 2.

4.7. Morphology of Emission Lines

Below we discuss some features that are apparent in our images of the N76 region shown in Figure 1.

Sharp and bright eastern edge. In most of the ionized gas emission lines, there is a brightness gradient with a northeastern sharp edge compared to a fainter and more diffuse southwestern edge. This is especially prominent in the lower ionization lines such as [S III]. We test how the brightness gradient impacts the Cloudy modeling in Appendix A.2. Modeling each individual side suggests a density difference of order ± 2 cm^{-3} from the best density in the radially averaged models or a typical density difference between each side of approximately 20%–30%.

Potential spiral structure. In some of the high ionization lines, particularly [O IV] and [S IV], there appears to be a "pinwheel" spiral structure emanating from AB7. The spiral has a single arm beginning at the location of AB7 and coils eastward then westward, ending about 10 pc away from AB7. This structure is also present in narrowband optical line imaging of HeII 4686 Å from Nazé et al. (2003). Spirals in WR-O star binaries have been seen before in dust emission (e.g., Tuthill et al. 1999; Lau et al. 2022) caused by the interacting stellar winds and the orbits of the binary. Spiral features are typically detected in the dust continuum of carbon-rich WC stars, but a spiral structure was reported in a nitrogen-rich star similar to the WR in AB7 in the radio continuum likely due to synchrotron emission (Rodríguez et al. 2020). This suggests that although the presence of dust helps illuminate a spiral pattern, it is intrinsic to binary systems and also present in other tracers. The spiral features documented in the literature, however, are on the scale of hundreds or thousands of AUs rather than the $\sim$10 pc feature we see in N76. The wind-collision zone where a spiral structure is expected for AB7 is $\sim$2 au in size, and therefore unresolved in our data. Nevertheless, it is possible that the high ionization lines of N76 show an imprint of the spiral motions from past stellar wind collisions in the central region, which then expand with the wind. Alternatively, the suggestive spiral structure may be coincidental and due to density gradients throughout the photoionized gas.

Dense knot. In the southeastern edge of N76 there is a bright knot of emission seen across the Spitzer IRS low ionization emission lines (and especially prominent in the [Si II] line). Previous work studying N76 suggests that this dense region is an independent compact HII region occasionally referred to as a "high excitation blob" (Heydari-Malayeri et al. 2001; Nazé et al. 2003). These are very dense, small regions that are associated with young massive stars beginning to leave their natal molecular cloud. Figure 7 shows the highly excited molecular gas in this blob, both in the H_2 quadrupole transitions as high as S(7) and a small clump of CO (2–1) (Tokuda et al. 2021). There are two possible ionizing sources for this compact region, including a Be star (Wisniewski & Bjorkman 2006) and a candidate young stellar object (Bolatto et al. 2007). It is unclear

whether either of these stars can power the ionization seen in this clump. Alternatively, it is possible that this feature is simply a dense blob of gas irradiated by AB7 and shocked by the HII region expansion.

4.8. Tentative [S I] Detection in the Center of N76

One peculiar detection from Spitzer IRS is a spectral line at 25.25 μm in the center of N76 that we tentatively identify as [S I]. The spectrum of this line can be seen in Figure 2 and the image in Figure 1. Our fitting procedure from PAHFIT identifies a spectral line between 25.2 and 25.3 μm throughout the central region of N76. The neutral sulfur line is directly in the middle of this range, at 25.245 μm. Using the NIST atomic spectral database, the nearest possible spectral lines correspond to Mg II at 25.05 μm and Si I at 25.38 μm. The redshift of these wavelengths due to the systemic velocity of the SMC is 0.01 μm. The average uncertainty PAHFIT reports on this spectral line wherever there are detections is 0.017 μm, which corresponds to $\sim$10% of the wavelength step between spectral pixels in this region of the LL1 map (0.178 μm).

The existence of neutral sulfur (or for that matter any line corresponding to ions found in neutral gas, such as Mg II and Si I) in the center of such a high ionization HII region is a mystery since neutral sulfur should be ionized quickly near such a hot and luminous star. Indeed, `Cloudy` predicts a total of 0.0005×10^{-15} W m^{-2} for the total [S I] intensity, which is almost 4 orders of magnitude fainter than the observed total flux of 1.04×10^{-15} W m^{-2}. The radial profile `Cloudy` predictions are also many orders of magnitude fainter than the observed flux, predicting an average of $\sim 10^{-13}$ W m^{-2} sr^{-1} compared to the observed $\sim 10^{-9}$ W m^{-2} sr^{-1} radial profile. If the line is confirmed as [S I], then it is the first detection of such a feature in the center of the highly irradiated environment of a WR nebula. Previous observations show [S I] resides in dense, neutral gas and can be produced through fast, dissociative J-shocks (Haas et al. 1991; Rosenthal et al. 2000). These observations, however, consistently show the presence of other neutral lines, such as H_2 and [O I]. In N76, there is no corresponding neutral emission where we observe [S I], making the production of this line a mystery. We explore possible explanations for this emission in Section 5.2.

5. Discussion

5.1. Ionized Gas Contributions to the Neutral Lines: [Si II], [C II], and [O I]

The ions and atoms that can exist in the neutral gas, Si^+ and C^+, have ionization potentials less than that of hydrogen, but their next ionization stage is above or close to 13.6 eV. The emission from [Si II] and [C II] can therefore be present in both the neutral and ionized gas phases. For [O I], the ionization potential of oxygen (13.618 eV) is very close to that of hydrogen and facilitates a very efficient charge-exchange reaction, ensuring that there is very little [O I] emission associated with the ionized gas. Although this work is focused on modeling only the ionized gas, understanding the proportion the ionized gas contributes to the overall intensity of the neutral-dominated lines is of interest for using these lines as neutral gas tracers. Our `Cloudy` simulations were designed to end at the ionization front, the position where the ionized gas transitions into fully neutral gas. To match the method in Cormier et al. (2019), we compute the contribution the neutral gas has on [Si II] and [C II] by defining a more conservative "end" of the ionized gas region as the point in which the electron fraction and proton fraction are equal to 0.5. We use this value to define the end of the ionized gas region for the following calculations.

As described in Section 4.4, the `Cloudy` models underpredict the emission from [O I] and [C II] that is observed in the direction of the nebula, because the neutral gas regions that surround the ionized gas but are not included in our `Cloudy` models contribute the bulk of the emission in these lines. In contrast, the [Si II] intensity is well matched to the predicted emission from ionized gas in the `Cloudy` models, suggesting a substantial amount of [Si II] is produced at the edge of the HII region itself and therefore not outside the HII region in the PDR. We quantify this by calculating the fraction of the intensity originating from the ionized gas for these lines in our models by defining the end of the ionized gas region as the point where the electron and neutral fraction are equal to 0.5. We find that for N76 91% of the [Si II] emission originates from the ionized gas while the [C II] has an ionized gas contribution of 3%. Cormier et al. (2019) use their `Cloudy` models of the Dwarf Galaxy Survey (DGS) to perform a similar calculation and report that $\lesssim$10% of the [C II] and $\lesssim$40% of [Si II] emission originates from the HII regions. Although we see a much higher HII region contribution to the [Si II] emission in N76 than in the galaxy-wide integrated measurements in the DGS, keep in mind that N76 is a WR nebula and thus may not be representative of most HII regions.

5.2. Production of [S I] in the Center of N76

We discussed in Section 4.8 the surprising identification of a line in the central regions of N76 as neutral sulfur. Below we go over some possible ideas about the origin of this transition.

Velocity shifted [O IV] *emission*: The nearest emission line in wavelength to our possible [S I] emission that is bright and clearly identified in N76 is [O IV] at 25.93 μm. We considered whether the line we identified as [S I] could be high velocity [O IV] emission. The velocity required to shift [O IV] to the observed wavelength of 25.25 μm is 7,600 km s^{-1}. While the WR and O stars in AB7 produce stellar winds, the speed of these winds is below 2000km s^{-1} (Shenar et al. 2016). The X-ray emission observed in N76, resulting from the colliding WR and O star winds, also implies a wind speed of 2000km s^{-1} (Guerrero & Chu 2008). Thus it is extremely unlikely that the emission is [O IV] shifted to 25.25 μm. Further, the wind would have to be asymmetric, since we do not see a corresponding redshifted component. Moreover, instead of discrete components, we would expect a symmetric, broadened [O IV] profile because the emission should be optically thin.

Dust destruction through shocks from stellar winds: The main mystery of the origin of [S I] at the center of this nebula is how sulfur can remain in a neutral state where ionized species caused by >55 eV photons are also observed. It is possible that the winds and radiation from AB7 can shock the surrounding dust, destroy dust grains, and move their constituent atoms, including neutral sulfur, into the gas phase. We then observe the [S I] emission before neutral sulfur is ionized into higher states. Most previous detections of [S I] are associated with shocks (e.g., Haas et al. 1991; Rosenthal et al. 2000; Neufeld et al. 2009; Simpson 2018) and shocks provide a mechanism to both release neutral sulfur material from the dust grains into the gas phase and to excite [S I] emission.

We evaluate whether this is possible by performing a back-of-the-envelope calculation. First, we estimate the timescale it would take to ionize sulfur in the hard radiation field of AB7. We integrate the ionizing spectrum over the ionization potential of sulfur (10.36 eV) to find the rate of sulfur-ionizing photons at a given distance of the [S I] emitting region. We calculate a timescale of 1.7 yr to ionize sulfur after assuming a cross section of 3×10^{-18} cm^{-3} (Draine 2011) and a radius of 10 pc. We next calculate the mass of neutral sulfur that must be replenished within this time. From the observed [S I] intensity we find the column density by assuming collisional excitation and use the equation given in Crawford et al. (1985), a critical density for collisions with e^- of $n = 1.55 \times 10^5$ cm^{-3} (Draine 2011), a spontaneous decay rate of $A = 1.40 \times 10^{-3}$ s^{-1} (Froese Fischer et al. 2006), a temperature of $T = 1.4 \times 10^4$ K, an abundance of 3.89×10^{-6} (Russell & Dopita 1992), and a density of $n = 40$ cm^{-3}. The density is chosen by assuming a strong shock wave will have four times the density of the preshocked medium of 10 cm^{-3} (e.g., Draine 2011). We calculate a column density of $N_{S^0} = 4.7 \times 10^{14}$ cm^{-2} and consequently a mass of $M_{S^0} = 3.7 \times 10^{-2}$ $M_\odot$ over a 10 pc radius. Thus our estimate suggests that 3.7×10^{-2} $M_\odot$ of sulfur will need to be lifted off of destroyed dust grains every 1.7 yr. Given the low abundance of sulfur relative to other elements that make the bulk of the dust mass (C, Si, O), this represents a very large dust mass destroyed every year, and it seems impossible this reservoir would exist over the life of the nebula (or be in some way replenished by the central source mass-loss rate). Further, there is no signature of other neutral species besides [S I] near the center of the nebula to support the scenario that dust destruction from shocks could produce the neutral sulfur. We would also expect that the other neutral species present in dust are also at the central part of nebula, which is not the case.

We note that if the [S I] emission is produced through dust destruction due to shocks from stellar winds, there would likely be a substantial amount of [Fe II] emission produced from the same mechanism since iron is heavily depleted in dust. The 25.9 μm blend of [O IV] 25.89 μm emission and [Fe II] 25.99μm described in Section 2.7 may therefore have a substantial contribution from [Fe II] 25.99 μm. However, since the [Fe II] 17.93 μm line is not detected and we predict <5% of the 25.9 μm line flux is from [Fe II], we conclude that the dust destruction scenario is unlikely.

Artifact in Spitzer IRS Data: The feature at 25.25 μm has multiple detections through the spectral slit scans and is not a one-time, random anomaly with the data. We instead explore two detector effects associated with Spitzer IRS data that can manifest as spurious spectral features and explain how they are unlikely to cause the possible [S I] feature at 25.25 μm. The IRS Handbook reports that spectral "ghost" features have appeared near extremely bright spectral lines in the short–high (SH) module near the 12.8 μm [Ne II] line (Simpson et al. 2007; IRS Instrument Team & Science User Support Team 2012). However, it is extremely unlikely that the 25.25 μm feature is a ghost of the 25.9 μm [O IV] line as the IRS Handbook specifically reports that no similar features had been found for the long–low (LL) module that covers the 25.25 μm line. The ghost features manifest in the SH module due to order mixing in the cross-disperser and there are no equivalent order-sorting filters for the LL module. Further, the ghost features that appear in the SH module are symmetric across the [Ne II] line due to the smearing of the flux on the plane of the slit and are also 0.5%–1% of the total flux of the line. The [S I] 25.25 μm feature observed in N76 is completely asymmetric, does not appear as a smeared feature on the slit plane, and is 5% of the total [O IV] flux, therefore strengthening the position that it is unlikely for the [S I] line to be a ghost feature of [O IV]. The other possible artifact we explore is spectral fringing, reported in the IRS handbook to be associated with the LL module where the 25.25 μm line is found. Spectral fringing manifests as residual nonsinusoidal wiggles in the IRS spectrum and begins at ~20 μm (IRS Instrument Team & Science User Support Team 2012). This fringing was more prevalent earlier in the Spitzer mission and has been seen in objects such as M82 and Cassiopeia A (Beirão et al. 2008; Smith et al. 2009). In these objects, the fringes are in a continuous pattern from 20–30 μm, are 1%–2% of the flux, and are coincident with the continuum and correlated with its brightness. The 25.25 [S I] μm feature in N76 is therefore unlike these spectral fringes because only a single feature appears in the spectrum, not the continuous pattern seen in all other cases. It is also a factor of 2 or more brighter than the fringe features and the [S I] line is not spatially correlated with the continuum. Therefore, we conclude that the 25.25 μm line is likely not due to a Spitzer IRS artifact, but future observations (such as with JWST) will be needed to confirm and characterize this curious line.

Unidentified spectral line: We used the NIST atomic spectral database to search for lines near the 20.0–20.5 μm range and did not identify any possible candidates besides [S I] (see discussion in Section 4.8). It is possible that the 25.25 μm emission originates from a molecular compound, but a molecule would have similar difficulties surviving the intense radiation field of AB7. Instead of [S I], however, this line could be an unidentified spectral line that corresponds to a very high ionization state not in the NIST catalog.

5.3. Physical Conditions in N76

Figure 8 presents how the electron temperature and electron density vary for each constant hydrogen density model as a function of physical distance from AB7. The electron density is slightly higher at the center of N76, due to the contribution from the He^{++} region that forms around very hot WR stars (see also the sixth panel in Figure 6). In our constant hydrogen density modeling, n_e stays constant up to the ionization front, where the gas transitions from ionized to neutral hydrogen. Overall, the electron density ranges from $n_e \sim 4$–12 cm^{-3} The temperature profile is smooth distribution, with a central peak near the edge of the photoionized region reaching 22,000–24,000 K, which then stays approximately constant at around 14,800 K until reaching hydrogen ionization front. Note that the inner regions close to the star are simply a cavity of radius 10 pc in the photoionization models, so the precise details of the transition between shock-ionized and photoionized gas are not accurately represented in these models.

The ratio of [S III] 18 μm/[S III] 33 μm also provides an estimate for n_e of an H II region. However, this ratio is only sensitive to gas with densities $n_e > 100$ cm^{-3}(Dudik et al. 2007), thus it does not probe the less dense ionized gas in N76. Our photoionization modeling of N76, however, is able to explore a wider region of parameter space than line ratios alone. Figure 8 shows how dramatically the size of the HII region changes for small changes in hydrogen density, illustrating the usefulness of spatially resolved data for characterizing HII regions.

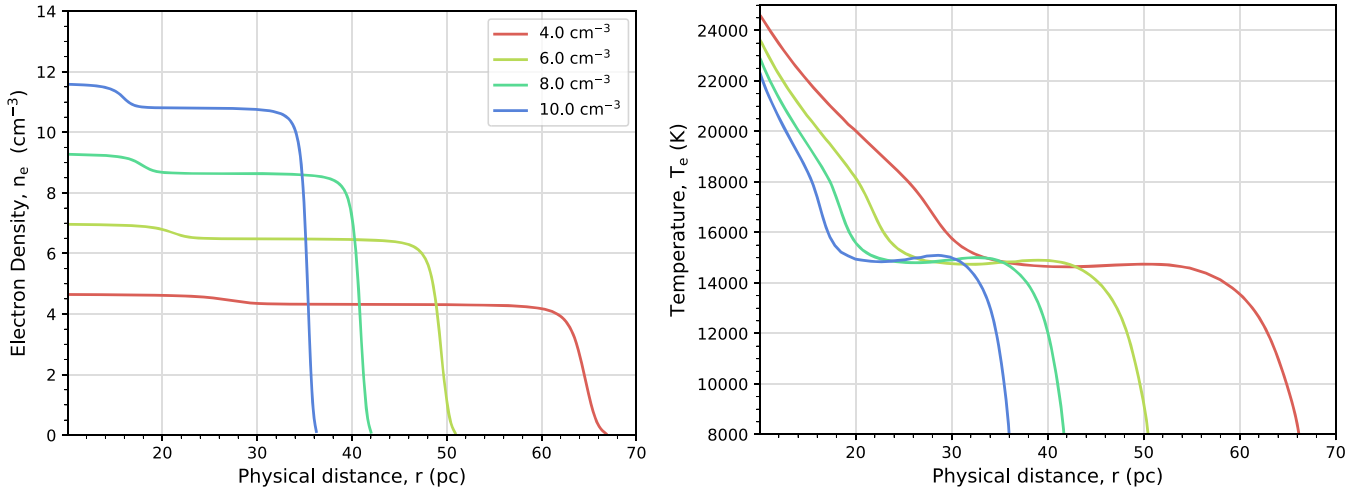

Figure 8. The electron temperature and density for the constant density `Cloudy` models as a function of physical distance away from AB7. Colors follow the same scheme as in Figure 3.

We also calculate the ionization parameter, U, defined as the dimensionless ratio of the hydrogen-ionizing photons to the total hydrogen density. This parameter is often used to characterize HII regions, and is defined as

$$U = \frac{Q(H)}{4\pi r_o^2 n(H) c}, \quad (4)$$

where r_o is the ionized region radius in units of cm, n(H) is the total hydrogen number density in units of cm^{-3}, c is the speed of light, and Q(H) is the number of hydrogen-ionizing photons emitted by the central source per second. The ionization parameter we measure for N76 ranges from $U = 1.7 \times 10^{-2}$ to $U = 7.1 \times 10^{-2}$, which is quite high and comparable to the massive H II region 30 Doradus (see Figure 9). The high radiation fields of AB7 and relatively low density of N76 explain that N76 has a high ionization parameter, even with a single ionization source.

We also note that the `Cloudy` models presented in this work are radiation-bounded, which are defined as HII regions wherein `Cloudy` models end at the ionization front and do not allow appreciable ionizing photons to escape. The `Cloudy` models presented here are an idealized case and represent the average of N76, but it is likely that some parts of the HII region are matter-bounded while others are radiation-bound. The southwestern edge of N76, for example, is much more diffuse than the rest of the nebula, which can allow ionizing photons to escape. A similar morphology is found in N76's HII region neighbor, the supergiant HII region N66 (Geist et al. 2022).

5.4. N76 in Context

The N76 nebula is unique for its very luminous central ionizing source, low density (∼10 cm^{-3}), and consequent large (∼40 pc) size. In order to compare it to other HII regions, we examine our results through two different lenses: observations of the ionized gas in low-metallicity dwarf galaxies, and in-depth studies of WR nebulae.

5.4.1. Comparison with Other Low-metallicity Systems

The largest study focused on understanding the properties of the mid-infrared transitions from gas in low-metallicity systems is the

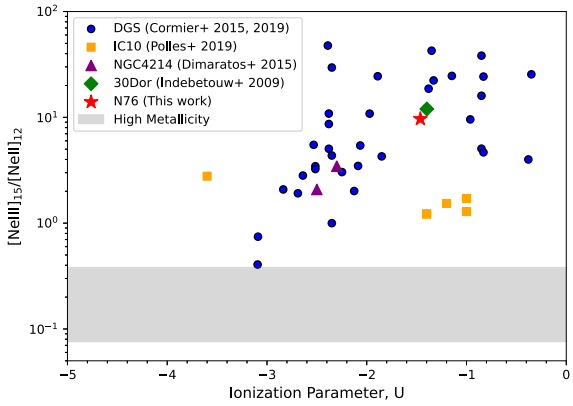

Figure 9. Comparing the [Ne III] 15 μm/[Ne II] 12 μm ratio to the ionization parameter of a variety of low-metallicity systems, including the Dwarf Galaxy Survey (Cormier et al. 2015, 2019), IC10 (Polles et al. 2019), NGC 4214 (Dimaratos et al. 2015), 30 Doradus (Indebetouw et al. 2009), and N76 (this work). These studies include a mixture of integrated data from entire galaxies (DGS), to individual measurements in divided regions of these galaxies (IC10 and NGC 4214), to single H II regions (N76 and 30 Dor). Overall, the [Ne III] 15 μm/[Ne II] 12 μm ratio shows that the low-metallicity systems plotted have much harder radiation fields than the averages shown for the higher-metallicity galaxies from Dale et al. (2009) and Inami et al. (2013).

Dwarf Galaxy Survey (DGS), which modeled IR observations of 48 nearby galaxies using `Cloudy` (Cormier et al. 2015, 2019). The results of DGS made considerable progress in the understanding of ionized gas properties in low-metallicity systems, but the majority of the sample consists of modeling an unresolved spectrum of each galaxy using a single or two-component Cloudy model. While recent, follow-up studies use a topological model to infer the statistical properties of the multiphase ISM from the unresolved data (Lebouteiller & Ramambason 2022; Ramambason et al. 2022, 2024), this work instead focuses on the nearby HII region N76 as it is fully resolved and contains a single, well-characterized ionization source. The models of N76 presented here provide an ideal case study to understand the impact WR stars have in low-metallicity environments, which are often characterized by active star formation and can contain a large number of WR stars (e.g., Izotov et al. 1997).

We compare the ionized gas properties found in the large surveys of dwarf galaxies below. Cormier et al. (2019) report

electron densities that range $n_e = 10^{0.5}$–$10^{3.0}$ cm^{-3} and ionization parameters of $\log U = -3.0$ to -0.3 with a correlation such that the highest U values are found in the lowest metallicity galaxies. This trend is also seen in the BCD galaxies analyzed in Hunt et al. (2010), where they report elevated [Ne III]/[Ne II], [S IV]/[S III], and [O IV]/[Si II] ratios when compared to higher-metallicity counterparts, indicative of harder radiation fields at low metallicities. Additionally, Hunt et al. (2010) report electron densities ranging from $n_e =$ 30–600 cm^{-3} through the [S III] 18 μm/[S III] 33 μm ratio. These two programs focused on analyzing spatially unresolved infrared spectroscopy of galaxy-wide measurements in order to form conclusions about the global ionized gas properties in dwarf galaxies. With a metallicity of 12 + log(O/H) ∼8.0, N76, as part of the SMC, falls at the median of the metallicity ranges investigated in these studies. The resolved measurements of N76 are well in the range of the globally integrated properties determined by these surveys, although the electron density in N76 is at the lower boundary found in these studies. This suggests that the brightest HII regions can dominate the excitation properties of the ISM in the ionized gas of these galaxies.

We also compare N76 to photoionization modeling studies of nearby dwarf galaxies that are more spatially resolved than those just described. To be consistent, all of these studies are done using similar IR spectroscopic observations and modeled with the Cloudy photoionization code. Indebetouw et al. (2009) model 30 Doradus in the Large Magellanic Cloud (LMC), the largest supergiant HII region in the nearby Universe. They find a relatively high electron density, $n_e =$ $10^{2.4}$–$10^{2.7}$cm^{-3} and a hard radiation field with $\log U =$ -1.7 to -1.3. Similarly, Polles et al. (2019) investigate the ionized gas in five individual star-forming clumps in IC10, and their Cloudy modeling indicates $n_e = 10^{2.0} - 10^{2.6}$ cm^{-3} and $\log U = -3.8$ to -1.0. Lastly, Dimaratos et al. (2015) focus their study on NGC 4214 and identify a separate central and southern star-forming region, calculating lower densities of $n_e = 440$ and $n_e = 170$, respectively, and ionization parameters of $U = -2.3$ and $U = -2.7$. Taken as a whole, N76 has a lower electron density than found in those objects, with somewhat larger ionization parameters.

In order to summarize the infrared Cloudy modeling results across these different surveys and studies, we plot the [Ne III] 15 μm/[Ne II] 12 μm and the Cloudy model ionization parameter, U, in Figure 9. This ratio traces the intensity of the radiation field and, in principle for a single main sequence star hardness should correlate well with U. We also plot a summary of the [Ne III] 15 μm/[Ne II] 12 μm ratio from a sample of high metallicity galaxies (Dale et al. 2009; Inami et al. 2013). While these analyses did not produce an ionization parameter, we do show their range in [Ne III] 15 μm/[Ne II] 12 μm line ratio. We confirm that the higher-metallicity galaxies have a much lower [Ne III] 15 μm/[Ne II] 12 μm line ratio than the low-metallicity systems. N76 and 30 Doradus are at the upper third of the observed line ratio, with [Ne III] 15 μm/[Ne II] 12 μm ∼10–15, indicating hard radiation fields in these HII regions. Many of the galaxies in the DGS sample have a similar ionization parameter and line ratio as these highly energetic H II regions, suggesting that conditions in these galaxies may be very similar to the resolved studies of N76 and 30Dor.

When examining scales of ∼200 pc, Cormier et al. (2019) find evidence of additional, low ionization components of ionized gas from their Cloudy models. Similarly, Polles et al. (2019) and Dimaratos et al. (2015) find excess emission of [Ne II] that they attribute to a diffuse ionized gas component. In N76, our Cloudy models also underpredict [Ne II], providing more evidence for an additional low ionization source that fuels the diffuse ionized gas in these galaxies.

5.4.2. Comparison with Other WR Nebulae

Most well-studied WR nebula are defined as bubble nebulae, characterized by thin ionized shells covering a large cavity, excavated by the strong stellar winds of the central WR star. Optical IFU measurements of the Milky Way WR nebula NGC 6888 show a three-shell structure centered around a 400 pc evacuated cavity: an elliptical inner broken shell formed by shocks from interactions between the WR and supergiant winds, an outer spherical shell that represents the windblown bubble, and a skin of ISM material surrounding the nebula (Fernández-Martín et al. 2012). Through photoionization modeling, Fernández-Martín et al. (2012) calculate an electron density of $n_e = 400$ cm^{-3} for the outer windblown bubble shell. Infrared spectroscopy described in Rubio et al. (2020) characterizes NGC 6888 further, corroborating the density found for the outer shell in Fernández-Martín et al. (2012) and identifying the density of the ISM skin as $n_e = 180$ cm^{-3}.

The overall morphological picture of NGC 6888 is not dissimilar to that of N76: a wind-shocked inner cavity caused by the powerful stellar winds of the WR star that transitions into a photoionized gas region and the surrounding ISM. However, N76 has a much smaller cavity (10 pc in our models compared to 400 pc), a lower-density photoionized region with $n_e = 4$–10 cm^{-3}, and this photoionized shell is rather thick compared to the cavity size (35 pc). These differences may be related to the age of N76. Shenar et al. (2016) estimate that AB7 is 3.4 Myr old, 1.3 Myr younger than WR 136 that powers NGC 6888 (Moore et al. 2000). The size of a stellar windblown bubble directly correlates with its age (Weaver et al. 1977; Freyer et al. 2003, 2006), suggesting that the younger N76 nebula will be smaller than NGC 6888. Observations of WR nebulae in the LMC show the traditional bubble structure, i.e., a large cavity with a thin, photoionized shell of material in the majority of nebulae (Hung et al. 2021).

Since the regions around WR nebulae contain material blown off by the powerful stellar winds of the star, their abundances can be enhanced, yielding elevated nitrogen abundances in those with a central WN star (e.g., Fernández-Martín et al. 2012; Stock & Barlow 2014). AB7 contains a WN4-type star, but we do not have a nitrogen spectral line to probe the nitrogen abundance. The abundances described in Table 2 do a satisfactory job of predicting the emission line surface brightness so we do not have evidence of elemental enhancement in N76. Optical spectroscopy of N76 by Nazé et al. (2003), however, shows a 40% elevated N/O ratio compared to global SMC values, suggesting that the chemical makeup of N76 is influenced by AB7.

6. Summary and Conclusions

We use Spitzer IRS spectroscopic maps of mid-infrared transitions and Cloudy to model the photoionization in the HII region N76 in the Small Magellanic Cloud. The ionization source is AB7, a binary composed of a WN4 nitrogen-rich WR and an O6 I supergiant star, and we use PoWR models

(Todt et al. 2015) that estimate its SED and luminosity (Shenar et al. 2016). AB7 contains one of the hottest WR stars in the SMC. We assume the N76 nebula is spherically shaped and project the predicted Cloudy line surface brightness as a function of distance to the source on the plane of the sky. We focus our study on emission from the ionized gas. The results from the photoionization models match the spatially resolved images of most ionized emission lines measured from Spitzer IRS and Herschel PACS observations, with just density as the free parameter. Our conclusions are as follows:

1. Comparing the models to the observed spatial distribution of the measured emission line brightness allows us to determine much more precise densities than just using the total line intensity (Figure 3 and Table 1).
2. Constant density Cloudy photoionization models reproduce most of the ionized gas emission line intensity distributions ([S III], [Ne III], [S IV], [Ne V], [O IV], and [O III]) for a narrow hydrogen density between $n_{\rm H} = 4\,{\rm cm}^{-3}$–$10\,{\rm cm}^{-3}$ (Figure 3).
3. The Cloudy photoionization models require a 10 pc cavity of hot, shocked plasma originating from a stellar windblown nebula in order to predict the spatial distribution of the ionized gas emission lines (Weaver et al. 1977; Freyer et al. 2003, 2006).
4. The high ionization lines, [O IV] and [Ne V] ($E_{\rm ion} > 50\,{\rm eV}$), are well predicted through the Cloudy models using the SED modeled in Shenar et al. (2016). The flux of these lines is highly sensitive to changes in the high-energy tail of the WR SED.
5. The neutral-dominated emission lines (lines coming from ionic species with an ionization potential less than hydrogen, 13.6 eV), can originate from both the ionized gas and the neutral gas. Our modeling finds that very little of the observed [C II] emission comes from the ionized gas (<5%), while most (91%) of the [Si II] emission can be produced in the transition from the HII region to PDR.
6. The [Ne II] line is underpredicted in our Cloudy models, suggesting the excess emission may arise from the diffuse ionized gas not associated with N76 (e.g., Dimaratos et al. 2015; Cormier et al. 2019; Polles et al. 2019).
7. We observe a feature at 25.25 μm that we tentatively identify as [S I] in the high ionization zone of the N76 nebula (see Figure 1). We explore possible causes for [S I] and alternative possibilities for the line in Section 5.2, including the possibility of producing neutral sulfur from dust destruction. None of these satisfactorily explains the line.
8. The physical conditions of N76 derived from the Cloudy models characterize a hot HII region with a maximum electron temperature range from $T_e \sim 22{,}000$–$24{,}000$K, a relatively small density range of $n_e \sim 4$–$12\,{\rm cm}^{-3}$, and high ionization parameters of $\log(U) = -1.15$to -1.77 (Section 5.3).
9. Low-metallicity galaxies have harder radiation fields than their higher-metallicity counterparts. The N76 region has a similar ionization parameter to samples of low-metallicity galaxies, suggesting that the bright HII regions dominate the spectrum of individual galaxies (see Figure 9).

Our work shows that just photoionization from low-metallicity WR stars can produce appreciable [O IV] and [Ne V] emission in the surrounding ISM. Thus N76 is a vital case study in determining the role of WRs in producing large fluxes of high ionization ions ($E_{\rm ion} > 50$ ev) found in low-metallicity Extreme Emission Line Galaxies (EELG) and BCD galaxies (e.g., Thuan & Izotov 2005; Izotov et al. 2012; Kehrig et al. 2015, 2018; Leitherer et al. 2018; Izotov et al. 2021; Olivier et al. 2022). Due to the rarity of WRs in population synthesis modeling (e.g., Leitherer et al. 2014), WR stars are often ruled out as a contributor to the high ionization lines. Our work suggests that the choice of the WR model can make a significant impact on the high-energy tail of the SED and consequently the amount of [Ne V] and [O IV] produced, suggesting that special care should be taken when modeling WR stars in unresolved systems.

Acknowledgments

We would like to thank T. Shenar for providing the SED of AB7 from Shenar et al. (2016). We thank K. Tokuda for providing the ALMA data from Tokuda et al. (2021) in Figure 7. We would also like to thank the anonymous referee for providing feedback that greatly improved the manuscript. E.T. would like to thank Ramsey Karim, Rebecca Levy, Carolyn Volpert, and Laura Lenkíc for many helpful discussions related to the manuscript.

E.T. and A.D.B. acknowledge support from NSF-AST2108140 and NASA ADAP 80NSSC19K1015. R.I. acknowledges support from NSF-AST2009624. M.R. wishes to acknowledge support from ANID(CHILE) through FONDECYT grant No1190684 and partial support from ANIDA Basal FB210003.

Software: astropy (The Astropy Collaboration 2013, 2018, 2022), CUBISM (v1.8; Smith et al. 2007a), Tiny Tim (Krist et al. 2011), Cloudy (Ferland et al. 2017), PAHFIT (Smith et al. 2007b)

Appendix A
PSF Matching Procedure

We follow the procedure described by Aniano et al. (2011) to create custom convolution kernels that will transform an image with a narrower PSF to a broader PSF.

Mathematically, we generate a kernel, K, that when convolved transforms Ψ_B, the narrower PSF, to Ψ_A, the broader PSF:

$$\Psi_A = \Psi_B * K(B \rightarrow A). \tag{A1}$$

To calculate the convolution kernel, K, we take the Fourier Transform (FT) and solve:

$$K(B \rightarrow A) = {\rm FT}^{-1}\left({\rm FT}(\Psi_B) \times \frac{1}{{\rm FT}(\Psi_A)}\right). \tag{A2}$$

Computing this kernel numerically while ensuring its accuracy and stability requires several steps outlined in Aniano et al. (2011) and are summarized below for completeness.

A.0.1. Preparing the PSFs

The IRS PSFs are from version 2.0 of the Spitzer Tiny Tim software.[9] We create model PSFs for the full wavelength range of IRS, 5–38 μm. We note that these are simulated PSFs and

[9] https://irsa.ipac.caltech.edu/data/SPITZER/docs/dataanalysistools/tools/contributed/general/stinytim/

there are some differences between the predicted PSF for IRS and the measured PSF from calibration stars, but these differences are negligible for our application (Pereira-Santaella et al. 2010). The PSFs range in pixel scale and image size, depending on the module. In order to calculate the convolution kernel, K, we regrid all PSFs to a common pixel scale of $0\farcs2$ and an image size of 1859×1859 pixels. The PSF matching algorithm outlined in Aniano et al. (2011) works best when the PSFs are rotationally symmetric. We circularize the PSFs by rotating the PSF 14 times and averaging after each rotation in order to make the final PSF invariant for any angle that is a multiple of $360^\circ/2^{14} = 0\fdg022$.

A.0.2. Creating the Convolution Kernel

We compute the Fourier Transform (FT) of the narrower PSF, Ψ_B, and the broader PSF, Ψ_A. We use the `PYTHON` package `FFTPACK` for all FT calculations. The FT of the target PSF is in the denominator (see Equation (A2)) and will amplify any small high-frequency components of the FT when creating the convolution kernel, K. We account for this by introducing a low-pass filter, f, in kernel construction:

$$f(k) = \begin{cases} 1 & \text{for } k \leqslant k_L \\ \frac{1}{2} \times \left[1 + \cos\left(\pi \times \frac{k - k_L}{k_{\rm H} - k_L}\right)\right] & \text{for } k_L \leqslant k \leqslant k_{\rm H} \\ 0 & \text{for } k_{\rm H} \leqslant k \end{cases} \tag{A3}$$

where k is the spatial frequency in the Fourier domain, $k_{\rm H}$ is the high-frequency cutoff for the filter, and $k_L = 0.7 \times k_{\rm H}$ is the low-frequency cutoff. We create the convolution kernel by modifying Equation A2 with the low-pass filter:

$$K(B \rightarrow A) = {\rm FT}^{-1}\left({\rm FT}(\Psi_B) \times \frac{1}{{\rm FT}(\Psi_A)} \times f(k)\right). \tag{A4}$$

repeating the process by looping over the narrower PSFs for Ψ_B. Lastly, we normalize the kernel to unity to ensure flux conservation.

A.0.3. Testing the Kernel

We test the convolution kernel for accuracy and stability through the metrics defined by Aniano et al. (2011). The convolution of the narrower PSF, Ψ_B, and the kernel, K $(B \rightarrow A)$, should reproduce the broader PSF Ψ_A (see Equation A1). Further, kernels with many negative values, which redistribute flux, can be unstable. Aniano et al. (2011) define two parameters, D (their Equation (20)), the integral of the difference between the convolved PSF and the target PSF, and W^-, a sum of the negative values in the kernel, to evaluate the kernels. We calculate these metrics and find very low values for D (< 0.01 for all kernels) and satisfactory values for W^- (ranges between 0.2 and 1.0). Aniano et al. (2011) report that $W^- < 1.2$ is stable. Further, the value chosen for the filtering function $k_{\rm H}$ affects these metrics, where an increase in k leads to a lower D but a higher W^-. When constructing kernels for each wavelength, we use a range of $k_{\rm H}$ values and select a $k_{\rm H}$ with the minimum of both W^- and D. The $k_{\rm H}$ filtering value ranges from 0.7 to 1.0 for the final convolution kernels.

A.0.4. The Final PSF-matched Images

We produce two sets of PSF-matched line images: one that provides maximum uniform resolution by matching to the PSF of the [Si II] transition (our longest wavelength line), and one that matches everything to a $12''$ Gaussian for ease of comparison with other data. In our analysis, we use the $12''$ Gaussian PSF. The [Si II] 34.8 μm line has the broadest PSF out of the spectral lines detected with Spitzer IRS with an FWHM of $7\farcs6$. We match each narrower IRS PSF to the PSF of the [Si II] line. Then, we create and apply a convolution kernel to go from the [Si II] PSF to a 2D Gaussian PSF. We find that a 2D Gaussian with an FWHM of $12''$ best matches the [Si II] PSF while balancing kernel stability.

Each emission line image is convolved with its custom kernel using the `ASTROPY` package `CONVOLUTION`. We then regrid each image to the coordinates of the [Si II] image to match its pixel scale and simplify the analysis. For the analysis, we also mask nonphysical bright artifacts and the emission from the SNR E0102-72. We use $12''$ Gaussian PSF-matched final images for the analysis in this work. Note that Figure 1 presents the original resolution images to show the maximum detail in the morphology of N76.

In addition to creating the PSF-matched line maps that are described in Section 2.1, we also produce a PSF-matched cube for the full IRS spectrum, including all orders: SL1, SL2, LL2, and LL1. We follow the same procedure on each frame of the original data cubes. A spectrum of the central position of the N76 nebula from the PSF-matched cube is presented in Figure 2.

We PSF match the IRS Spitzer data, but not the Herschel PACS images (see Section 2.2). The emission line images from PACS have larger PSFs that would degrade too much the resolution of the IRS maps if we were to match each image to the largest Herschel PSF.

Appendix B
Effect of Asymmetries in N76

In order to compare the `Cloudy` models directly to various emission lines in N76, we need to assume spherical symmetry. However, it is clear that the images of the emission lines show spatial asymmetries in Figure 1. The eastern side of N76 is brighter in almost every IR line and the western edge is less well defined, with more diffuse, extended features. To explore how these asymmetries affect the `Cloudy` modeling, we show here the results for a narrow strip that intersects with the AB7 and designate it as the central point. We then sample the surface brightness to the left (eastern edge) and right (western edge) of the strip and report it in Figure 10.

The asymmetric profiles show that the western edge prefers a lower-density model in almost all cases (except for [O I], [C II], and [Ne II]). The idealized symmetric model presented in the radial profiles in Figure 3 is simply an average of these two sides. The difference between these densities is relatively low, however, with the higher density side preferring a model only 4 $\rm cm^{-3}$ larger. This is typically a $\pm$20%–30% change in the result of the spherically symmetric modeling.

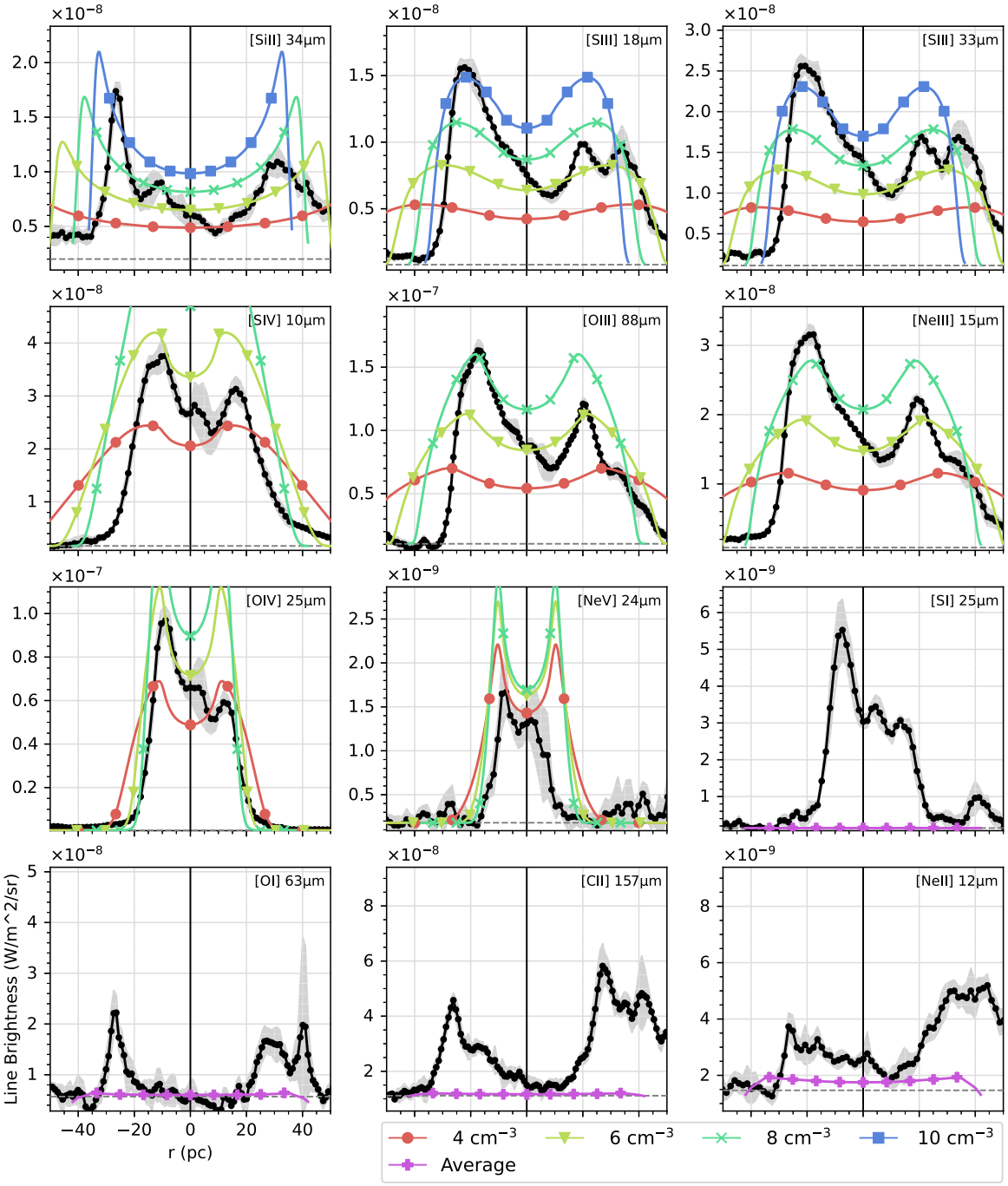

Figure 10. The surface brightness distribution of emission lines taken as a strip across the nebula with AB7 in the center and the eastern and western edges on the left and right hand of the plot, respectively. This shows the asymmetry of N76, where the eastern edge is brighter than the western side. The `Cloudy` models prefer a slightly lower density for the western side.

ORCID iDs

Elizabeth Tarantino https://orcid.org/0000-0003-1356-1096
Alberto D. Bolatto https://orcid.org/0000-0002-5480-5686
Rémy Indebetouw https://orcid.org/0000-0002-4663-6827
Mónica Rubio https://orcid.org/0000-0002-5307-5941
Karin M. Sandstrom https://orcid.org/0000-0002-4378-8534
J.-D T. Smith https://orcid.org/0000-0003-1545-5078
Daniel Stapleton https://orcid.org/0009-0000-4156-5604
Mark Wolfire https://orcid.org/0000-0003-0030-9510

References

Aniano, G., Draine, B. T., Gordon, K. D., & Sandstrom, K. 2011, PASP, 123, 1218
Astropy Collaboration, Price-Whelan, A. M., Lim, P. L., et al. 2022, ApJ, 935, 167
Astropy Collaboration, Price-Whelan, A. M., Sipőcz, B. M., et al. 2018, AJ, 156, 123
Astropy Collaboration, Robitaille, T. P., Tollerud, E. J., et al. 2013, A&A, 558, A33
Atek, H., Siana, B., Scarlata, C., et al. 2011, ApJ, 743, 121
Baldovin-Saavedra, C., Audard, M., Güdel, M., et al. 2011, A&A, 528, A22

Baldwin, J. A., Phillips, M. M., & Terlevich, R. 1981, PASP, 93, 5
Beirão, P., Brandl, B. R., Appleton, P. N., et al. 2008, ApJ, 676, 304
Berg, D. A., Chisholm, J., Erb, D. K., et al. 2019, ApJL, 878, L3
Blair, W. P., Morse, J. A., Raymond, J. C., et al. 2000, ApJ, 537, 667
Bolatto, A. D., Simon, J. D., Stanimirović, S., et al. 2007, ApJ, 655, 212
Chevalier, R. A. 2005, ApJ, 619, 839
Chu, Y. H. 1981, ApJ, 249, 195
Chu, Y. H., Treffers, R. R., & Kwitter, K. B. 1983, ApJS, 53, 937
Conti, P. S., & Massey, P. 1989, ApJ, 337, 251
Cormier, D., Abel, N. P., Hony, S., et al. 2019, A&A, 626, A23
Cormier, D., Madden, S. C., Lebouteiller, V., et al. 2015, A&A, 578, A53
Crawford, M. K., Genzel, R., Townes, C. H., & Watson, D. M. 1985, ApJ, 291, 755
Crowther, P. A., & Hadfield, L. J. 2006, A&A, 449, 711
Dale, D. A., Cohen, S. A., Johnson, L. C., et al. 2009, ApJ, 703, 517
Dennefeld, M., & Stasińska, G. 1983, A&A, 118, 234
Dimaratos, A., Cormier, D., Bigiel, F., & Madden, S. C. 2015, A&A, 580, A135
Draine, B. T. 2011, Physics of the Interstellar and Intergalactic Medium (Princeton, NJ: Princeton Univ. Press)
Dudik, R. P., Weingartner, J. C., Satyapal, S., et al. 2007, ApJ, 664, 71
Dufour, R. J. 1984, in IAU Symp. 108, Structure and Evolution of the Magellanic Clouds, ed. S. van den Bergh & K. S. D. de Boer (Dordrecht: Reidel), 353
Ferland, G. J., Chatzikos, M., Guzmán, F., et al. 2017, RMxAA, 53, 385
Fernández-Martín, A., Martín-Gordón, D., Vílchez, J. M., et al. 2012, A&A, 541, A119
Foellmi, C., Moffat, A. F. J., & Guerrero, M. A. 2003, MNRAS, 338, 360
Freyer, T., Hensler, G., & Yorke, H. W. 2003, ApJ, 594, 888
Freyer, T., Hensler, G., & Yorke, H. W. 2006, ApJ, 638, 262
Froese Fischer, C., Tachiev, G., & Irimia, A. 2006, ADNDT, 92, 607
Galliano, F., Nersesian, A., Bianchi, S., et al. 2021, A&A, 649, A18
Garnett, D. R., Kennicutt, R. C., Jr., Chu, Y.-H., & Skillman, E. D. 1991, ApJ, 373, 458
Geist, E., Gallagher, J. S., Kotulla, R., et al. 2022, PASP, 134, 064301
Gräfener, G., Koesterke, L., & Hamann, W. R. 2002, A&A, 387, 244
Guerrero, M. A., & Chu, Y.-H. 2008, ApJS, 177, 216
Haas, M. R., Hollenbach, D., & Erickson, E. F. 1991, ApJ, 374, 555
Haffner, L. M., Dettmar, R. J., Beckman, J. E., et al. 2009, RvMP, 81, 969
Hainich, R., Ramachandran, V., Shenar, T., et al. 2019, A&A, 621, A85
Hainich, R., Rühling, U., Todt, H., et al. 2014, A&A, 565, A27
Hamann, W. R., & Gräfener, G. 2003, A&A, 410, 993
Hamann, W. R., & Gräfener, G. 2004, A&A, 427, 697
Hayashi, I., Koyama, K., Ozaki, M., et al. 1994, PASJ, 46, L121
Henize, K. G. 1956, ApJS, 2, 315
Heydari-Malayeri, M., Charmandaris, V., Deharveng, L., et al. 2001, A&A, 372, 495
Hollenbach, D., & McKee, C. F. 1989, ApJ, 342, 306
Hung, C. S., Ou, P.-S., Chu, Y.-H., Gruendl, R. A., & Li, C.-J. 2021, ApJS, 252, 21
Hunt, L. K., Thuan, T. X., Izotov, Y. I., & Sauvage, M. 2010, ApJ, 712, 164
Hurley, J. R., Pols, O. R., & Tout, C. A. 2000, MNRAS, 315, 543
Inami, H., Armus, L., Charmandaris, V., et al. 2013, ApJ, 777, 156
Indebetouw, R., de Messières, G. E., Madden, S., et al. 2009, ApJ, 694, 84
IRS Instrument TeamScience User Support Team 2012, IRS Instrument Handbook, IPAC, v.5.0, 145
Izotov, Y. I., Foltz, C. B., Green, R. F., Guseva, N. G., & Thuan, T. X. 1997, ApJL, 487, L37
Izotov, Y. I., Thuan, T. X., & Guseva, N. G. 2021, MNRAS, 508, 2556
Izotov, Y. I., Thuan, T. X., & Privon, G. 2012, MNRAS, 427, 1229
Jenkins, E. B., & Wallerstein, G. 2017, ApJ, 838, 85
Kaufman, M. J., Wolfire, M. G., & Hollenbach, D. J. 2006, ApJ, 644, 283
Kehrig, C., Vílchez, J. M., Guerrero, M. A., et al. 2018, MNRAS, 480, 1081
Kehrig, C., Vílchez, J. M., Pérez-Montero, E., et al. 2015, ApJL, 801, L28
Krist, J. E., Hook, R. N., & Stoehr, F. 2011, Proc. SPIE, 8127, 81270J
Lancaster, L., Ostriker, E. C., Kim, J.-G., & Kim, C.-G. 2021, ApJ, 914, 90
Lau, R. M., Hankins, M. J., Han, Y., et al. 2022, NatAs, 6, 1308
Lebouteiller, V., Bernard-Salas, J., Brandl, B., et al. 2008, ApJ, 680, 398
Lebouteiller, V., & Ramambason, L. 2022, A&A, 667, A34
Lee, M.-Y., Stanimirović, S., Ott, J., et al. 2009, AJ, 138, 1101
Leitherer, C., Byler, N., Lee, J. C., & Levesque, E. M. 2018, ApJ, 865, 55
Leitherer, C., Ekström, S., Meynet, G., et al. 2014, ApJS, 212, 14
Leroy, A., Bolatto, A., Stanimirovic, S., et al. 2007, ApJ, 658, 1027
Maseda, M. V., van der Wel, A., da Cunha, E., et al. 2013, ApJL, 778, L22
Moore, B. D., Hester, J. J., & Scowen, P. A. 2000, AJ, 119, 2991
Nazé, Y., Rauw, G., Manfroid, J., Chu, Y. H., & Vreux, J. M. 2003, A&A, 408, 171
Neufeld, D. A., Nisini, B., Giannini, T., et al. 2009, ApJ, 706, 170
Neugent, K. F., Massey, P., & Morrell, N. 2018, ApJ, 863, 181
Niemela, V. S., Massey, P., Testor, G., & Giménez Benítez, S. 2002, MNRAS, 333, 347
Olivier, G. M., Berg, D. A., Chisholm, J., et al. 2022, ApJ, 938, 16
Parkin, E. R., & Pittard, J. M. 2008, MNRAS, 388, 1047
Pereira-Santaella, M., Diamond-Stanic, A. M., Alonso-Herrero, A., & Rieke, G. H. 2010, ApJ, 725, 2270
Poglitsch, A., Krabbe, A., Madden, S. C., et al. 1995, ApJ, 454, 293
Polles, F. L., Madden, S. C., Lebouteiller, V., et al. 2019, A&A, 622, A119
Ramambason, L., Lebouteiller, V., Bik, A., et al. 2022, A&A, 667, A35
Ramambason, L., Lebouteiller, V., Madden, S. C., et al. 2024, A&A, 681, A14
Rigby, J. R., Bayliss, M. B., Gladders, M. D., et al. 2015, ApJL, 814, L6
Rodríguez, L. F., Arthur, J., Montes, G., Carrasco-González, C., & Toalá, J. A. 2020, ApJL, 900, L3
Roman-Duval, J., Gordon, K. D., Meixner, M., et al. 2014, ApJ, 797, 86
Rosenthal, D., Bertoldi, F., & Drapatz, S. 2000, A&A, 356, 705
Rubio, G., Toalá, J. A., Jiménez-Hernández, P., et al. 2020, MNRAS, 499, 415
Russell, S. C., & Dopita, M. A. 1990, ApJS, 74, 93
Russell, S. C., & Dopita, M. A. 1992, ApJ, 384, 508
Sander, A., Shenar, T., Hainich, R., et al. 2015, A&A, 577, A13
Sandstrom, K. M., Bolatto, A. D., Bot, C., et al. 2012, ApJ, 744, 20
Sandstrom, K. M., Bolatto, A. D., Draine, B. T., Bot, C., & Stanimirović, S. 2010, ApJ, 715, 701
Sandstrom, K. M., Bolatto, A. D., Stanimirović, S., van Loon, J. T., & Smith, J. D. T. 2009, ApJ, 696, 2138
Schaerer, D., & Stasińska, G. 1999, A&A, 345, L17
Schaerer, D., & Vacca, W. D. 1998, ApJ, 497, 618
Senchyna, P., Stark, D. P., Vidal-García, A., et al. 2017, MNRAS, 472, 2608
Shenar, T., Hainich, R., Todt, H., et al. 2016, A&A, 591, A22
Simpson, J. P. 2018, ApJ, 857, 59
Simpson, J. P., Colgan, S. W. J., Cotera, A. S., et al. 2007, ApJ, 670, 1115
Smith, J. D. T., Armus, L., Dale, D. A., et al. 2007a, PASP, 119, 1133
Smith, J. D. T., Draine, B. T., Dale, D. A., et al. 2007b, ApJ, 656, 770
Smith, J. D. T., Rudnick, L., Delaney, T., et al. 2009, ApJ, 693, 713
Sokal, K. R., Johnson, K. E., Indebetouw, R., & Massey, P. 2016, ApJ, 826, 194
Stevens, I. R., Blondin, J. M., & Pollock, A. M. T. 1992, ApJ, 386, 265
Stock, D. J., & Barlow, M. J. 2014, MNRAS, 441, 3065
Tchernyshyov, K., Meixner, M., Seale, J., et al. 2015, ApJ, 811, 78
Thuan, T. X., & Izotov, Y. I. 2005, ApJS, 161, 240
Toalá, J. A., Guerrero, M. A., Ramos-Larios, G., & Guzmán, V. 2015, A&A, 578, A66
Toalá, J. A., Marston, A. P., Guerrero, M. A., Chu, Y. H., & Gruendl, R. A. 2017, ApJ, 846, 76
Todt, H., Sander, A., Hainich, R., et al. 2015, A&A, 579, A75
Tokuda, K., Kondo, H., Ohno, T., et al. 2021, ApJ, 922, 171
Tuthill, P. G., Monnier, J. D., & Danchi, W. C. 1999, Natur, 398, 487
Vermeij, R., & van der Hulst, J. M. 2002, A&A, 391, 1081
Vink, J. S., de Koter, A., & Lamers, H. J. G. L. M. 2001, A&A, 369, 574
Weaver, R., McCray, R., Castor, J., Shapiro, P., & Moore, R. 1977, ApJ, 218, 377
Wisniewski, J. P., & Bjorkman, K. S. 2006, ApJ, 652, 458
Wolfire, M. G., Hollenbach, D., McKee, C. F., Tielens, A. G. G. M., & Bakes, E. L. O. 1995, ApJ, 443, 152
Wolfire, M. G., McKee, C. F., Hollenbach, D., & Tielens, A. G. G. M. 2003, ApJ, 587, 278
Wu, Y., Charmandaris, V., Hao, L., et al. 2006, ApJ, 639, 157